5

Physics of Quasi-Monoenergetic Laser-Plasma Acceleration of Electrons in the Blowout Regime

Serguei Y. Kalmykov[1], Bradley A. Shadwick[1],
Arnaud Beck[2] and Erik Lefebvre[2]
[1]*Department of Physics and Astronomy, University of Nebraska – Lincoln, Lincoln*
[2]*CEA, DAM, DIF, Arpajon F-91297*
[1]*USA*
[2]*France*

1. Introduction

Progress in the technology of optical pulse amplification (Herrmann et al., 2009; Ross et al., 2000; Spence et al., 1991; Strickland & Mourou, 1985) has made sub-50 fs pulse length, 0.1–10 Hz repetition rate, multi-terawatt (TW) lasers available to university-scale laboratories. These new instruments, accessible to a large community of researchers, revolutionized experiments in relativistic nonlinear optics (Mourou et al., 2006), and enabled the compact design of plasma-based particle accelerators (Esarey et al., 2009; Tajima & Dawson, 1979). Owing to continuous improvements in laser systems and gas target technology (Semushin & Malka, 2001; Spence & Hooker, 2001), stable generation of well-collimated, quasi-monoenergetic, hundred-megaelectronvolt (MeV)-scale electron beams from millimeter to centimeter-length plasmas has become experimentally routine (Brunetti et al., 2010; Faure et al., 2006; Hafz et al., 2008; Leemans et al., 2006; Maksimchuk et al., 2007; Malka et al., 2009; Mangles et al., 2007; Osterhoff et al., 2008). These beams have been used for a broad range of technical and medical physics applications – γ-ray radiography for material science (Glinec et al., 2005; Ramanathan et al., 2010), testing of radiation resistivity of electronic components used in harsh radiation environments (Hidding et al., 2011), efficient on-site production of radioisotopes (Leemans et al., 2001; Reed et al., 2007), and radiotherapy with tunable, high-energy electrons (DesRosiers et al., 2000; Glinec et al., 2006; Kainz et al., 2004). Their unique properties – femtosecond (fs)-scale duration and multi-kiloampere current (Buck et al., 2011; Lundh et al., 2011) – are clearly favorable for ultrafast science applications, such as high-energy radiation femtochemistry (Brozek-Pluska et al., 2005), spatio-temporal radiation biology and radiotherapy (Malka et al., 2010), and compact x-ray sources (Fuchs et al., 2009; Grüner et al., 2007; Hartemann et al., 2007; Kneip et al., 2010; Pukhov et al., 2010; Rousse et al., 2007; Schlenvoigt et al., 2008). The current record of accelerated electron energy is close to one gigaelectronvolt (GeV) (Clayton et al., 2010; Froula et al., 2009; Kneip et al., 2009; Leemans et al., 2006; Liu et al., 2011). Furthermore, ongoing introduction of sub-150 fs, compact, high repetition rate petawatt (PW) lasers (Aoyama et al., 2003; Gaul et al., 2010; Hein et al., 2006; Korzhimanov et al., 2011; Sung et al., 2010) opens possibilities beyond the GeV energy frontier (Gorbunov et al., 2005; Kalmykov et al., 2010a; Lu et al., 2007; Martins et al., 2010), enabling further steps towards practical designs of high-brightness x-

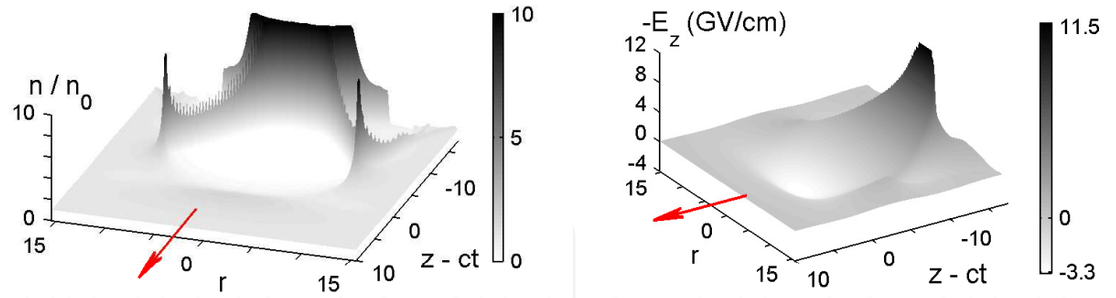

(a) Normalized electron density (b) Accelerating gradient, $-E_z$ (in GV/cm)

Fig. 1. Electron density bubble driven by the 70 TW laser pulse in a plasma of density $n_0 = 6.5 \times 10^{18}$ cm^{-3} (cf. Fig. 3(d.1)). The laser pulse (not shown) is centered at $z \approx ct$ and propagates in the direction indicated by the arrow. The wake bucket (plot (a)) is devoid of electrons; the peak of electron density at its rear is well above the cutoff value $10n_0$. The accelerating gradient (plot (b)) reaches 11.5 GV/cm at the rear of the bucket.

and γ-ray sources and compact high energy physics particle colliders (Schroeder et al., 2010). Success of these applications critically depends on high collimation and low energy spread of the multi-GeV beams. Presently, however, laser-plasma accelerators (LPAs) produce GeV-scale electrons with polychromatic energy distributions spanning from a few MeV to the maximum energy observed; sometimes with a quasi-monoenergetic feature at the high-energy end (Clayton et al., 2010; Froula et al., 2009; Kneip et al., 2009; Liu et al., 2011). In this Chapter, we explore the relationship between the electron beam quality and the nonlinear evolution of the accelerating structure – a three-dimensional (3-D) bucket of a strongly nonlinear, fully electromagnetic (EM) plasma wake – and propose dynamical scenarios to help reduce electron energy spread and suppress the poorly collimated polychromatic background.

In a modern LPA experiment, the ponderomotive force of a focused pulse produces a full cavitation of the surrounding electron fluid. All plasma electrons facing the pulse are expelled by the radiation pressure (whereas fully stripped ions remain immobile). Fields due to this charge separation attract bulk electrons to the axis, and their trajectories overshoot. The resulting closed cavity of electron density (the "bubble" (Pukhov & Meyer-ter-Vehn, 2002)) surrounded by a dense shell (sheath) of relativistic electrons encompasses the pulse and guides it over many Rayleigh lengths until depletion (Lu et al., 2007; Mora & Antonsen, 1996). Figure 1 presents one example of such fully cavitated bucket.

The bubble is a high-quality 3-D EM accelerating structure. Its longitudinally uniform but radially linear focusing gradient implies strict conservation of normalized transverse emittance. In addition, the accelerating field is radially uniform, which helps mitigate longitudinal emittance dilution (Lu et al., 2006; Rosenzweig et al., 1991). The bubble propagates with the group velocity of laser pulse in the plasma, which in a linear approximation can be expressed as $v_g = c(1 - \gamma_g^{-2})^{1/2}$, where c is a speed of light in vacuum, and $\gamma_g = \omega_0/\omega_{pe} \gg 1$ (here, ω_0 is the laser frequency, $\omega_{pe} = (4\pi e^2 n_0/m_e)^{1/2}$ is the Langmuir electron frequency, m_e is the electron rest mass, n_0 is the background electron density, and e is the electron charge). Therefore, even with the Lorentz factor γ_g approaching 100, the bubble remains a "slow" accelerating structure capable of trapping initially quiescent electrons from the ambient plasma (Kalmykov et al., 2010a; Lu et al., 2007; Martins et al., 2010). Single-shot

optical diagnostics, such as second harmonic generation from the sheath (Gordon et al., 2010; Helle et al., 2010) and frequency-domain holography/shadowgraphy (Dong et al., 2010a;b), show a direct correlation between the generation of collimated electron beams and bubble formation. Also, the moment of injection can be precisely identified (Thomas et al., 2007a). Electron self-injection greatly simplifies the experimental design enabling a single-stage acceleration with considerable flexibility in beam parameters.

The bubble shape and potentials are determined by the electron flow surrounding the cavitated area. The majority of electrons slip behind the bubble within a time interval close to the period of plasma oscillations, $\tau_p = 2\pi/\omega_{pe}$. This means that the bubble, on the whole, is a quasistatic structure (Lu et al., 2006; Mora & Antonsen, 1996). At the same time, the sheath electrons, exposed to the highest fields and preaccelerated to relativistic energies, stay with the bubble much longer (Kalmykov et al., 2011b). If the quasistatic bubble expands during their slippage time (satisfying semi-empirical condition discussed in section 2.1), the sheath electrons can penetrate into the bubble near its rear, synchronize with it (i.e. obtain the longitudinal momentum $p_{\|} \approx \gamma_g m_e c$), and then travel inside the cavity, continuously gaining energy (Kalmykov et al., 2011b). Diffraction of the driving laser pulse is usually sufficient to cause this kind of dynamic behavior (Kalmykov et al., 2009; Xu et al., 2005). Therefore, the quality of accelerated beam, sensitive to the details of self-injection process, appears to be tied to the self-consistent optical evolution of the driver.

Accelerated electrons eventually outrun the slow bubble. They exit the accelerating phase within a time interval $\tau_d = L_d/c$, where $L_d = (2/3)\gamma_g^2 R_b$ is the dephasing length, and R_b is the bubble radius. Acceleration until dephasing maximizes the energy gain, yielding $E_{\max} \approx 0.085\gamma_g^2 (k_p R_b)^2$ MeV, where $k_p = \omega_{pe}/c$ (Lu et al., 2007). Numerical simulations presented in this Chapter correspond to $\gamma_g \approx 16$, $k_p R_b \approx 5$, yielding $L_d \approx 1.7$ mm and $E_{\max} \approx 550$ MeV. In strongly rarefied plasmas, such as $\gamma_g \gg 3k_p R_b/4$, dephasing takes many Rayleigh lengths (this estimate implies that the laser pulse spot size approximately equals to the bubble radius). To propagate the pulse over this distance in a uniform background plasma, majority of modern experiments rely on a combination of relativistic and ponderomotive self-guiding (Hafizi et al., 2000; Ralph et al., 2009). The following dynamical scenario is usually the case. Upon entering the plasma, the pulse with $P/P_{\rm cr} \gg 1$ and $\tau_L < \tau_p$ self-focuses until full electron cavitation is achieved, and the charge-separation force of an electron density channel (bubble) balances the radial ponderomotive force; the pulse is then guided until depletion (here, $P_{\rm cr} = 16.2\gamma_g^2$ GW is the critical power for relativistic self-focusing (Sun et al., 1987)). The condition of the force balance matches the peak vector potential of the pulse (normalized to $m_e c^2/|e|$) to the bubble radius as $a_{\rm sg} \approx (k_p R_b/2)^2 \gg 1$ (Lu et al., 2007). Even though the bubble is a natural attractor for the relativistic laser-plasma dynamics (Gordienko & Pukhov, 2005), both transient dynamics *before* the onset of self-guiding (Kalmykov et al., 2010a) and the laser evolution *during* the self-guiding (Froula et al., 2009; Kalmykov et al., 2010a; 2011b; Kneip et al., 2009; Oguchi et al., 2008) may cause unwanted additional electron injection (dark current), degrading the beam quality. The lack of balance between the light pressure and charge-separation force makes the pulse spot size oscillate (Kalmykov et al., 2010a; Oguchi et al., 2008); self-steepening (Vieira et al., 2010) and depletion (Decker et al., 1996) gradually turn the pulse into a relativistically intense piston (Kalmykov et al., 2011b); and relativistic filamentation (Andreev et al., 2007; Kalmykov et al., 2010a; Thomas et al., 2007b; 2009) distorts the transverse profile of the pulse. Resulting deformations of the bubble, to which self-injection is extremely sensitive (Kalmykov et al., 2010b; 2011b), lead to the rapid degradation of electron beam quality (Froula et al., 2009; Kalmykov et al., 2010a; 2011b; Kneip et al., 2009; Martins et al., 2010). Novel optical diagnostics, such as frequency-domain

streak cameras (Dong et al., 2010b; Li et al., 2010; 2011), allow capturing the details of bubble evolution and associating them with the final quality of electron beam in a given experimental shot, providing necessary feedback for the real-time optimization. The combined effort of theory and experiment should thus be aimed at suppressing dark current through a proper optimization and control of laser pulse evolution without complicating the experimental design (ideally, involving a single laser pulse and a single gas target).

It has been understood that to reduce the nonlinear effects and stabilize the bubble during the pulse self-guiding, it is necessary to work with matched PW-class pulses in low-density plasmas, $\gamma_g > 35$ (Lu et al., 2007). At even lower densities, $\gamma_g > 100$, initial mismatching of the pulse (e.g. over-focusing) helps enforce and control the injection (Kalmykov et al., 2010b; 2011a). With $P \sim 10P_{cr}$, and $\tau_L < \tau_p/2$, the initially over-focused laser diffracts, the bubble expands, and electrons are injected continuously. When self-guiding sets in, the bubble stabilizes, and self-injection terminates. Secondary injection into the same bucket remains suppressed, and low-energy tails do not develop in the electron spectra. Electrons injected during the period of expansion travel deep inside the bucket and are continuously accelerated. At the same time, electrons injected late are located in the region of the highest accelerating gradient. They rapidly equalize in energy with earlier injected particles. Thus, a nanocoulomb (nC), quasi-monoenergetic bunch forms long before dephasing (Kalmykov et al., 2009; 2010b; 2011a). It can be further accelerated without emittance dilution, reaching multi-GeV energy near dephasing, keeping a few percent energy spread and a few mrad divergence. By varying plasma density and/or laser focusing geometry, one can control initial mismatching, changing the system behavior during the brief initial transient stage, thus precisely controlling the charge and emittance (Kalmykov et al., 2011a). High optical quality of the PW pulse is critically important for the realization of this scheme (Kalmykov et al., 2010a; Wang et al., 2011).

With a higher power ratio, $P/P_{cr} > 10$, and/or longer pulse, $\tau_L > \tau_p/2$, the described above scheme becomes compromised (Kalmykov et al., 2010a). The length of the transient stage increases, giving rise to multiple oscillations of the laser spot size and periodic injection (Kalmykov et al., 2010a), resulting in polychromatic electron energy distributions (Martins et al., 2010). At higher plasma densities, $\gamma_g < 20$, longitudinal deformation of the pulse becomes another source of the dark current (Kalmykov et al., 2011b). The leading edge of the pulse that pushes away plasma electrons rapidly accumulates frequency red-shift, and group velocity dispersion concurrently compresses the pulse (Fang et al., 2009; Faure et al., 2005; 2006; Pai et al., 2010; Vieira et al., 2010). Concomitant depletion of the leading edge further enhances the self-steepening effect (Decker et al., 1996; Lu et al., 2007). Initially smooth driver thus turns into a relativistically intense "piston", or a "snow-plow" that pre-accelerates and compresses the initially quiescent electron fluid. A large charge separation immediately behind the piston results in sheath electrons receiving strong longitudinal kick, increasing their inertia, and delaying their return to the axis. As a result, the bubble elongates, and massive, uninterrupted self-injection follows (Froula et al., 2009; Kalmykov et al., 2011b; Kneip et al., 2009). In spite of high injected charge, this scenario remains the same in both quasistatic and fully explicit, 3-D EM particle-in-cell (PIC) simulations (Kalmykov et al., 2011b). Beam loading (Rechatin et al., 2010; Tzoufras et al., 2009) becomes important only in the final stage of this process. Notably, in this situation, transverse matching of the pulse precludes neither periodic nor continuous injection (Martins et al., 2010), and thus does not help improve the beam characteristics. However, the dark current-free acceleration can be achieved even in these unfavorable regimes. Giving up acceleration until dephasing, and limiting the plasma length to one cycle of laser waist oscillation results in a

quasi-monoenergetic beam formation (Hafz et al., 2011; Kalmykov et al., 2009). This approach does not maximize electron energy and thus does not optimize the accelerator performance. However, high-quality, a few-hundred MeV electron beams with tunable parameters can be produced, which is valuable for applications. In addition, as we show in section 3, using a broad bandwidth, negatively chirped pulse may help compensate for the nonlinear red-shift and delay formation of the relativistic piston, thus reducing the amount of dark current.

In this Chapter, we elucidate the intrinsic connection of electron injection with the laser pulse optical evolution and demonstrate the mechanism of monoenergetic electron beam formation. We also discuss adverse scenarios of the pulse evolution leading to the continuous injection, and propose ways to mitigate them. To examine electron injection during various stages of laser pulse evolution in a single numerical experiment, we use two complementary simulation approaches. In section 2, we explain the physics, and develop the conceptual framework of the problem using the quasistatic, cylindrically symmetric, fully relativistic PIC code WAKE (Mora & Antonsen, 1997). A fully 3-D, non-averaged, dynamic test electron tracking module incorporated in WAKE (Kalmykov et al., 2009; Malka et al., 2001) emulates the non-quasistatic response of initially quiescent electrons to a high-frequency quasi-paraxial laser field and slowly varying EM plasma wakes. In section 2.5 we validate the test-particle results in a full 3-D PIC simulation using the code CALDER-Circ (Lifschitz et al., 2009).

The formation of a quasi-monoenergetic electron bunch during one period of laser spot oscillation is the subject of sections 2.1, 2.2, and 2.3. By analyzing quasistatic trajectories and using the results of test electron tracking in section 2.1, we identify precisely the injection candidates, collection volume, and evaluate the minimal bubble expansion rate for the initiation of self-injection. Formation of the quasi-monoenergetic beam during one period of the bubble size oscillation is described in section 2.2. Results of section 2.3 show that self-injection and subsequent acceleration of an electron require initial reduction of its moving-frame Hamiltonian. Laser pulse self-compression and resulting continuous injection are considered in section 2.4. In section 2.5, we validate the self-injection scenarios discussed in sections 2.1 – 2.4 in a CALDER-Circ simulation. We find that the test-particle modeling correctly identifies physical processes responsible for the initiation and termination of self-injection. Using our fast simulation toolkit (WAKE with test particles) and CALDER-Circ code, we explain in section 3 that laser self-compression and concomitant continuous injection can be suppressed by using a negatively chirped, broad bandwidth driver pulse. In section 4 we summarize the results and point out directions of future work.

2. Self-injection scenarios in the blowout regime

We study self-injection and acceleration of electrons until dephasing in a standard regime of LPA experiments at the University of Nebraska (Ramanathan et al., 2010). We examine various scenarios of injection and relate them to nonlinear dynamical processes involving the laser pulse. The quasistatic behavior of the bulk plasma makes it possible to elucidate the physics of self-injection using a conceptually simple and computationally efficient toolkit: a fully relativistic 3-D particle tracking module built into the cylindrically symmetric time-averaged (over ω_0^{-1}) quasistatic PIC code WAKE (Mora & Antonsen, 1997). WAKE uses an extended paraxial solver for the slowly varying laser pulse envelope, which preserves the group velocity dispersion in the vicinity of the carrier frequency and calculates precisely radiation absorption due to the wake excitation. Electron response to the time-averaged ponderomotive force is calculated assuming that *all* plasma electrons (macroparticles) eventually fall behind the bubble. This approach, termed the quasistatic

approximation (QSA), tremendously speeds-up the simulation, enabling serial runs and extensive parameter scans using small workstations. On the other hand, neglecting the long-term contribution of near-luminous-speed macroparticles traveling with the bubble prohibits self-consistent modeling of electron self-injection and trapping. To simulate self-injecton without compromising computational efficiency, we use test particles. The test-particle module is fully dynamic, making no assumption of cylindrical symmetry, and is not time-averaged. In particular, it takes into account the interaction of test electrons with the non-averaged, linearly polarized laser field with non-paraxial corrections (Quesnel & Mora, 1998). To capture the laser pulse interaction with non-quasistatic background electrons (and thus to model self-injection into non-stationary quasistatic wakefields), a group of quiescent test electrons is placed before the laser pulse at each time step. In this way, electron self-injection associated with bubble and driver evolution is separated from the effects brought about by the collective fields of the trapped electron bunch, i.e. from effects due to beam loading. This simulation approach allows us to fully characterize the details of self-injection process and relate them to the evolution of the laser and the bubble using a non-stationary Hamiltonian formalism (Kalmykov et al., 2010b; 2011b).

In the simulation, a transform-limited, linearly polarized Gaussian laser pulse with a full width at half-maximum in intensity $\tau_L = 30$ fs and central wavelength $\lambda_0 = 0.805$ μm is focused at the plasma border ($z = 0$) to a spot size $r_0 = 13.6$ μm, and propagates towards positive z. The plasma has a 0.5 mm linear entrance ramp followed by a 1.7 mm plateau. The length of the plateau is equal to the dephasing length. Plasma density, $n_0 = 6.5 \times 10^{18}$ cm^{-3}, corresponds to $\gamma_g = \omega_0/\omega_{pe} \approx 16.3$. The laser power is 70 TW, which yields $P/P_{cr} = 16.25$, a peak intensity at the focus 2.3×10^{19} W/cm^2, and normalized vector potential $a_0 = 3.27$. The WAKE simulation uses a grid $dr \approx 0.1k_p^{-1} \approx 0.21$ μm, with 30 macroparticles per radial cell, $d\xi = dr/3$ (where $\xi = z - ct$), and time step $dt = dz/c \approx 1.325\omega_0^{-1}$.

2.1 Injection candidates, collection volume, and minimal expansion rate to initiate injection

Upon entering the plasma, the laser pulse self-focuses and reaches the highest intensity at $z \approx 0.8$ mm. Full blowout is maintained over the entire propagation distance. Bubble expansion *and* electron injection begin soon after the laser pulse enters the density plateau. The wakefield potential, time-averaged (over ω_0^{-1}) Lorentz forces, electron density, and sample trajectories of macroparticles $r_i(\xi)$ are shown in Fig. 2 for the fully expanded bubble after 1 mm of propagation (cf. position (2) of Fig. 3).

The quasistatic electron density and number density of non-quasistatic test particles in (r, ξ) space are strikingly similar in Fig. 2(c). Thus, even though the macroparticles cannot be trapped, analysis of their trajectories helps identify the injection candidates, and specify the scenario of bubble evolution favorable for injection. This analysis also provides precise estimates of the collection volume and the bubble expansion rate necessary to initiate the injection. Each macroparticle can be put into one of three clearly defined groups [color coded in Figs. 2(d) – 2(f)]. The majority of electrons, viz. those expelled by the radiation pressure (black) and those attracted from periphery to the axis (green), are passing. They fall behind the bubble roughly within a time interval $\tau_b = L_b/c$ (where $L_b \approx 2R_b$ is the bubble length). The bulk plasma electrons thus obey the QSA restrictions exceptionally well, which enables precise WAKE modeling. Sheath electrons (red) are different; they may travel with the bubble over a long distance. Figure 2(e) shows that their slippage time,

$$T_{\text{slip}} = \int_0^{L_b} \frac{d\zeta}{c - v_z}, \tag{1}$$

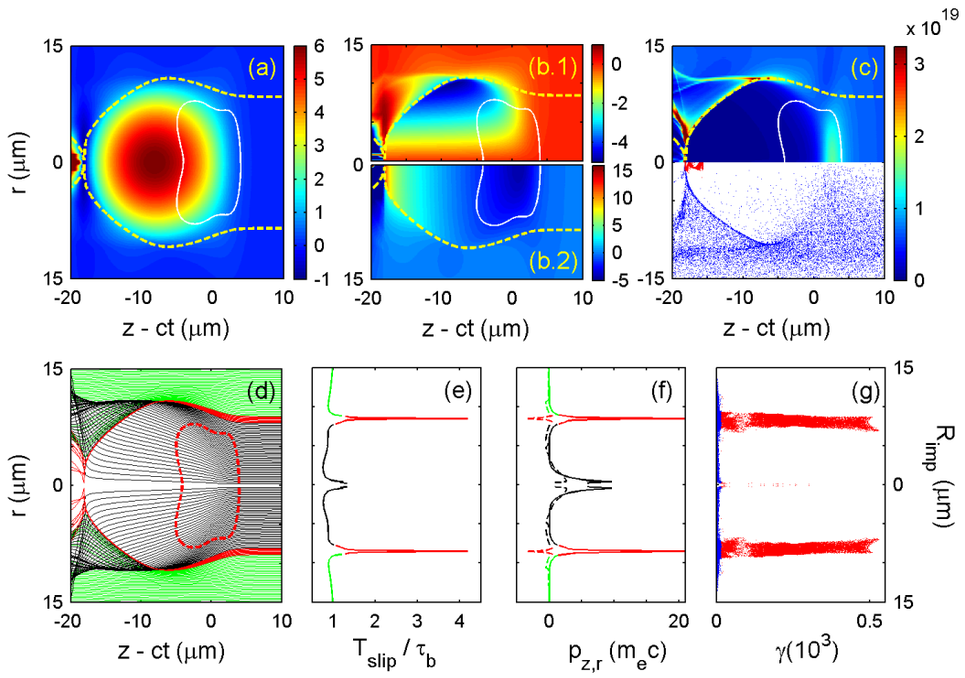

Fig. 2. Fully expanded bubble from the WAKE simulation (cf. position (2) of Fig. 3). Solid white and dashed red contours in panels (a–d) are the iso-contours of laser intensity at $\exp(-2)$ of the peak (the pulse propagates to the right). (a) Wake potential $\Phi = \phi - A_z$ in units $m_e c^2/|e|$. (b) Focusing ($-E_r + B_\theta$, top) and accelerating ($-E_z$, bottom) Lorentz forces (in GV/cm). (c) Top: the quasistatic electron density (in cm^{-3}). Bottom: radial positions of non-quasistatic test electrons. Red markers are the test particles with $\gamma > \gamma_\mathrm{g} = 16.3$. (d) Trajectories $r(\xi)$ of the quasistatic macroparticles. Green and black trajectories correspond to passing electrons. Red trajectories correspond to sheath electrons – injection candidates. (e) Normalized slippage time as a function of the impact parameter, $R_\mathrm{imp} = r(\xi \gg c\tau_L)$. (f) Longitudinal ($p_z$, solid line) and transverse (p_r, dashed line) momenta of macroparticles at the rear of the bubble (the point of trajectory crossing). Sheath electrons have the largest slippage time, and become relativistic before crossing the axis. The yellow dashed curve in panels (a–c) is a trajectory of the macroparticle with the greatest slippage time ("the innermost electron"). (g) Impact parameters of test electrons from panel (c) vs energy.

significantly exceeds τ_b (here, $\zeta = -\xi$, and $\zeta = L_b \approx 18\ \mu$m is the coordinate of the rear of the bubble). A yellow broken line in Figs. 2(a) – 2(c) shows the trajectory of the macroparticle with the largest slippage time, $T_\mathrm{slip} \approx 4.2\tau_b$. Figure 2(d) indicates that the sheath electrons originate from a hollow cylinder with a radius close to the laser pulse spot size. While slipping through the structure, they are exposed to the highest wakefields. At the rear of the bubble, they are strongly pre-accelerated in *both* longitudinal *and* transverse directions: Fig. 2(f) gives $p_{z\,\max} \approx 21 m_e c > \gamma_\mathrm{g} m_e c$, and $|p_{r\,\max}| \approx 4 m_e c$. The large longitudinal momentum of these electrons makes them the best injection candidates; their promotion to fully dynamic macroparticles may result in their self-injection and acceleration (Morshed et al., 2010).

Longitudinal synchronization of sheath electrons, $p_z \geq \gamma_\mathrm{g} m_e c$, is necessary and, in high-density plasmas (such as $\gamma_\mathrm{g} \approx k_p R_b$), also sufficient for their injection (Kostyukov et al., 2009). In the opposite limit of strongly rarefied plasmas, $\gamma_\mathrm{g} > 10 k_p R_b$, the sheath electrons do not

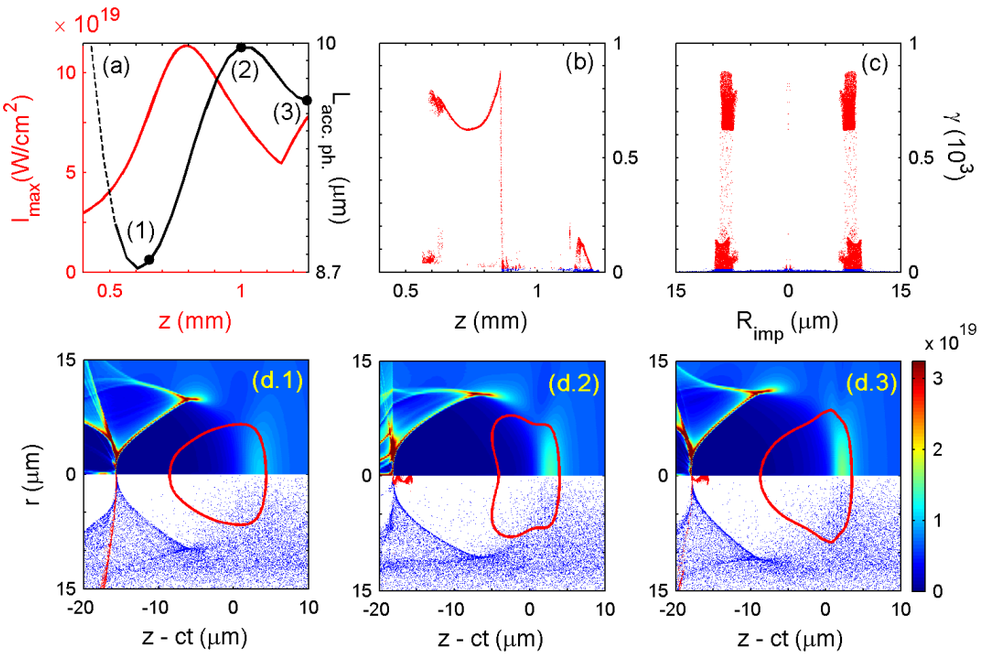

Fig. 3. Electron injection into the oscillating bubble. (a) Peak laser intensity (red) and length of the accelerating phase $L_{\text{acc.ph.}}$ (black) vs propagation distance; $L_{\text{acc.ph.}}$ is the distance between the positions of zero and peak accelerating gradient on axis – see Fig. 4(b). Panels (b) and (c): energy of test electrons vs their initial longitudinal (b) and radial (c) positions after one period of bubble size oscillation (cf. position (3) of panel (a)). (d.1) – (d.3) Quasistatic electron density in cm^{-3} (color map) and number density of non-quasistatic test particles (dots) corresponding to the positions (1) – (3) of the plot (a) (labeled accordingly). Red contour is an iso-contour of laser intensity at $\exp(-2)$ of the peak. Data from positions (1) – (3) are used to describe the process of monoenergetic electron bunch formation in Fig. 4.

synchronize with (and thus cannot be injected into) a non-evolving bubble (i.e. depending on variables r and ξ only); in this case, evolution of the bucket is vital for self-injection (Kalmykov et al., 2009; 2010a;b; 2011a). In the intermediate regime with $\gamma_g \approx 3.5 k_p R_b$ (which is the focus of this Chapter), longitudinal synchronization appears to be insufficient for injection. The sheath electrons crossing the axis have relativistic transverse momenta, and thus tend to exit the cavity in the radial direction. Such electrons have been earlier observed in the laboratory in the absence of any noticeable trapping (Helle et al., 2010; Kaganovich et al., 2008). To be injected (i.e. return to axis), the injection candidates must be confined into a focusing cavity *after* crossing the axis. To this effect, the bubble must continuously *expand*, changing its size by an appreciable fraction during the electron transit time T_{slip}. Energetic sheath electrons can then outrun the boundary of the bubble and stay inside long enough to *both* synchronize longitudinally *and* make a U-turn transversely. To separate the most energetic electrons from the sheath, elongation of the bubble over the slippage time has to exceed the sheath thickness Δ_{sh} at the rear of the bucket (Kalmykov et al., 2010b; 2011b),

$$\Delta L_b = L_b(t + T_{\text{slip}}) - L_b(t) \geq \Delta_{\text{sh}}, \tag{2}$$

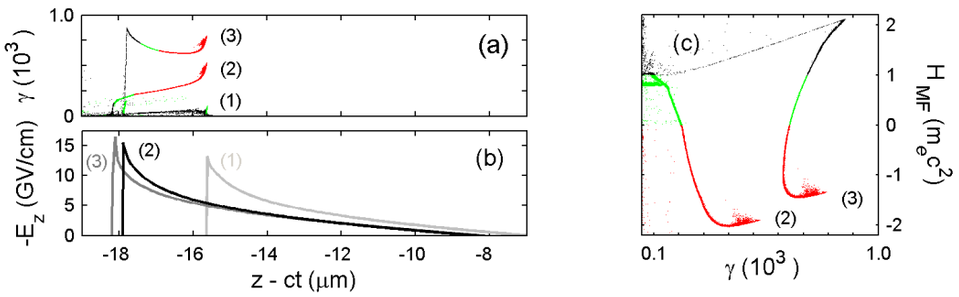

Fig. 4. Phase space rotation and formation of a quasi-monoenergetic bunch (Kalmykov et al., 2011b). (a) Phase space rotation of injected test electrons. Longitudinal phase space is shown at the positions (1)–(3) of Fig. 3(a). (1) Injection begins. (2) The bubble is fully expanded, injection stops, and phase space rotation begins. (3) The bucket slightly contracts. Electrons injected lately equalize in energy with those injected earlier. Quasi-monoenergetic bunch forms. Test electrons are color coded according to $H_{MF} < 0$ (red), $0 < H_{MF} < 1$ (green), $H_{MF} > 1$ (black). (b) Axial line-outs of the accelerating gradient (in GV/cm). (c) H_{MF} vs energy gain for the fully expanded (2) and contracted (3) bubble.

where the parameter $\Delta_{\rm sh}$ has to be found empirically from simulations. For the fully expanded bubble of Fig. 2, $\Delta L_b \approx 3\Delta_{\rm sh} \approx 0.5$ μm (the estimate obtained using Fig. 3(a)), which is sufficient to maintain the injection. Indeed, a group of test particles accelerated to $\gamma > \gamma_{\rm g}$ (red markers) can be seen at the base of the bubble in Fig. 2(c). Figure 2(g) indicates that, in agreement with earlier studies (Pukhov et al., 2010; Tsung et al., 2006; Wu et al., 2009), only electrons with impact parameters such that they enter the sheath are collected and accelerated. And, the condition (2) always holds, sometimes rather closely, when self-injection occurs in low-density plasmas, $\gamma_{\rm g} > 65$ (Kalmykov et al., 2009; 2010a;b; 2011a).

All accelerated electrons in Figs. 2(c,g) are collected from a cylindrical shell with thickness $\Delta R_{\rm coll} \approx 2$ μm and radius close to the laser spot size, $R_{\rm coll} \approx 8$ μm. The length of this hollow cylinder equals to the interval of bubble expansion from Fig. 3(a), $\Delta z_{\rm exp} \approx 400$ μm. This collection volume contains 2.6×10^{11} electrons – injection candidates (42 nC charge). To calculate the injected charge correctly, one has to take into account the self-fields of both sheath and recently trapped electrons near the base of the bubble, making resort to the fully kinetic simulations (Kalmykov et al., 2011b; Morshed et al., 2010). 3-D PIC simulation of section 2.5 shows that only 0.5% of particles from the collection volume are actually injected. Injection from a very narrow range of impact parameters, together with low collection efficiency in realistic PIC modeling, makes massive self-injection during the slippage time very unlikely. Injected particles thus remain the minority, and their contribution to the bubble evolution is insignificant. This justifies the quasistatic treatment of the plasma electrons making up the accelerating structure, and validates the test-particle model of self-injection process.

The background plasma is never perfectly uniform in the laboratory experiment. Localized density depressions, which may naturally occur in gas jet targets, can also cause electron self-injection (Hemker et al., 2002; Suk et al., 2001). Even if the driver evolution is negligible (as in the beam-driven case (Lu et al., 2006; Rosenzweig et al., 1991)), the bubble crossing a density down-ramp necessarily expands; if the ramp is longer than a slippage distance, $L_{\rm ramp} \gg cT_{\rm slip}$, then the bubble evolution is slow, and Eq. (2) applies. The bubble length in the non-uniform plasma is $L_b(z) = \kappa(2\pi/k_{p0})/\sqrt{\tilde{n}_e(z)}$, where the parameter $\kappa \sim 1$ is

determined empirically from simulations. Assuming a power-law density profile, $\tilde{n}_e(z) \equiv n_e(z)/n_0 = 1 - A[(z - z_{\rm in})/L_{\rm ramp}]^{\alpha}$, where $\tilde{n}_e(z < z_{\rm in}) = 1$, and $\tilde{n}_e(z > z_{\rm in} + L_{\rm ramp}) = 1 - A < 1$, and substituting $z - z_{\rm in} = cT_{\rm slip}$ into Eq. (2), we find the relation between the length of the ramp $L_{\rm ramp}$ and density depression A necessary to incur injection: $L_{\rm ramp} < cT_{\rm slip}[A\kappa\pi/(k_{p0}\Delta_{\rm sh})]^{1/\alpha}$. Using parameters of the bubble from Fig. 2, we find that a linear down-ramp with a 10% density depression may produce self-injection if $L_{\rm ramp} < 0.47$ mm. If the plasma density is more homogeneous than that, the self-injection into the bubble can be enforced by the pulse evolution only.

2.2 Self-injection into an oscillating bubble: formation of quasi-monoenergetic collimated electron beam

The first period of bubble size oscillations is displayed in Fig. 3. Figure 3(d.1) shows the bubble and the laser pulse at the beginning of bubble expansion (cf. position (1) of Fig. 3(a)); Fig. 3(d.2) at the end of expansion (cf. position (2) of Fig. 3(a)); and Fig. 3(d.3) at the end of oscillation period (cf. position (3) of Fig. 3(a)). The laser pulse entering the density plateau at $z = 0.5$ mm is longer than one-half of the electron plasma period, $\tau_L \approx 0.7\tau_p$. Its head, residing in an incompletely evacuated nonlinear channel, remains guided with an almost invariant spot size, $r(\xi \approx 0) \approx 6.5$ μm, whereas the tail, confined within an evacuated bubble, is strongly mismatched. Beating of the mismatched tail, causing alternating expansion and contraction of the bubble, are clearly seen in progression from Fig. 3(d.1) to 3(d.3).

Figure 3(a) shows that bubble expansion starts near the edge of the density plateau and continues until $z \approx 1$ mm. The bubble expands by 14% of its size over a 400 μm distance ($\sim$ 20 bubble lengths). Injection of non-quasistatic test electrons continues uninterrupted during this stage, and, as is clear from Fig. 4(a), their momentum distribution is continuous. Contraction of the bubble between $z = 1$ and 1.25 mm extinguishes injection and truncates the bunch: electrons injected at the very end of expansion are expelled. Particles remaining in the bucket are further accelerated. At this stage, the bunch becomes quasi-monoenergetic. According to Fig. 4(b), the longitudinally nonuniform, co-moving accelerating gradient changes insignificantly during the contraction. The tail of the bunch, constantly exposed to the highest gradient, equalizes in energy with earlier injected electrons (cf. position (3) of Fig. 4(a)). This rotation of longitudinal phase space, responsible for the formation of a quasi-monoenergetic bunch long before dephasing, is clearly different from that discussed in literature (Tsung et al., 2006). According to Figs. 3(b) and (c), electrons remaining in the bucket at the end of bubble contraction are collected during the interval of bubble expansion from a cylindrical shell with the radius close to the laser spot size. They form the bunch with the energy $E = 360^{+40}_{-20}$ MeV and 4.3 mrad divergence. *Therefore, limiting the plasma length to a single period of the bubble size oscillations gives a quasi-monoenergetic, collimated electron beam* (Hafz et al., 2011; Kalmykov et al., 2009).

2.3 Evolution of test electron Hamiltonian during injection

WAKE calculates all potentials directly, which makes the Hamiltonian analysis of test particle tracking straightforward. Using the definitions of normalized momentum $\mathbf{p} \equiv \mathbf{p}/(m_e c)$, wake potential $\Phi = |e|(\varphi - A_z)/(m_e c^2)$ (where ϕ is a scalar potential, and A_z is the longitudinal component of vector potential), envelope of the laser vector potential $\mathbf{a} \equiv |e|\mathbf{a}/(m_e c^2)$, and $\gamma_e = (1 + \mathbf{p}^2 + \mathbf{a}^2/2)^{1/2}$, we introduce the normalized time-averaged moving-frame (MF) Hamiltonian $H_{MF}(r, z, \xi) = \gamma_e + \Phi - p_z$. For the quasistatic macroparticles, $H_{MF} \equiv 1$ (Mora & Antonsen, 1997). Test electrons (which are not assumed to be quasistatic) move in explicitly time-dependent potentials; hence, H_{MF} changes in the course of propagation

according to $dH_{MF}/dt = \partial H_{MF}/\partial t$. For a test electron moving away from the bubble, $H_{MF} = \gamma_e + \Phi - p_z \to \sqrt{1+\mathbf{p}^2} - p_z > 0$. Hence, the electron is confined inside the bucket at all times (trapped) if the H_{MF} remains *negative* in the course of interaction. As soon as the bubble stabilizes, H_{MF} is conserved. All test electrons can be then divided into 3 groups: (1) $H_{MF} < 0$ — trapped; (2) $0 < H_{MF} < 1$ — injected (accelerated); and (3) $H_{MF} > 1$. All the three groups are represented in Fig. 4(a), where the phase space of test electrons is shown at the stationary points of full expansion (labeled (2)) and full contraction of the bubble (labeled (3)). Electron phase space for the fully expanded bubble shows that the bubble expansion causes a reduction in H_{MF} (Kalmykov et al., 2009; 2010b). The condition $H_{MF} < 1$ is thus *necessary* for injection and initial acceleration. For instance, it can be used for promotion of test electrons into the non-quasistatic electron beam particles in order to self-consistently incorporate beam loading into the model. Conversely, even minimal bubble contraction may raise H_{MF} significantly. Figure 4(c) shows that electrons with $0 < H_{MF} < 2$ are accelerated as effectively as those which are formally trapped. Hence, the natural evolution of the structure may result in violation of the sufficient trapping condition; this, however, does not disrupt acceleration with good collimation and low energy spread (Kalmykov et al., 2011b).

2.4 Continuous self-injection caused by self-compression of the driving pulse

Although a monoenergetic electron bunch forms early, the general experimental trend is to push the accelerator efficiency to the limit and use the entire dephasing length. Electron beam quality, however, can be compromised in this pursuit. The driver pulse evolves continuously, which may cause uninterrupted electron injection and emittance growth. Understanding the physical mechanism of continuous injection will help control the beam quality by limiting injection via a judicious choice of laser-plasma interaction geometry and target design (Kalmykov et al., 2011a) or by manipulating the phase and envelope of the incident pulse.

Running the simulation until the nonlinear dephasing limit, we find two distinct stages of the system evolution. Stage I, discussed above, corresponds to a single oscillation of the laser spot size and produces a monoenergetic electron bunch. Stage II is characterized by a gradual increase of laser intensity (up to 2×10^{20} W/cm^2) and a steady elongation of the bubble. Figure 5 shows that bubble elongation is accompanied by continuous injection and growth of the energy spread. At the end of the run, the number of continuously injected test electrons ($\gamma > \gamma_g$) is factor of 7.5 larger than the number of electrons in the leading quasi-monoenergetic bunch. Similar development of self-injection process has been reported elsewhere (Froula et al., 2009; Kneip et al., 2009). Figures 5(c.1) – 5(d.3) show that the asymmetric growth (elongation) of the bubble is accompanied by self-compression of the driver pulse from 25 to roughly 5.5 fs, and simultaneous 5-fold increase in intensity. The compressed pulse (relativistic piston) acts as a snow-plow. The ponderomotive push of its front pre-accelerates plasma electrons to $\gamma > \gamma_g$ and, as is seen in Figs. 5(c.2) and 5(c.3), creates a strongly compressed electron slab an order of magnitude denser than the ambient plasma. As a result of this strong charge separation, plasma electrons entering the sheath (as can be seen in Figs. 6(b) and 6(d)) are exposed to the positive electric field a factor 2.25 higher than in the case of smooth driver (Figs. 6(a) and 6(c)). Hence, upon passing the piston, sheath electrons receive a large kick in the backward direction, and quickly become relativistic, $p_z \approx -1.65 m_e c$ (in contrast to $-0.55 m_e c$ in the smooth driver case). Therefore, in the piston case, it takes nearly twice as long for the sheath electron to reach the point of return, $p_z = 0$, and to start getting accelerated; reaching the axis also takes longer time, which explains the bubble elongation.

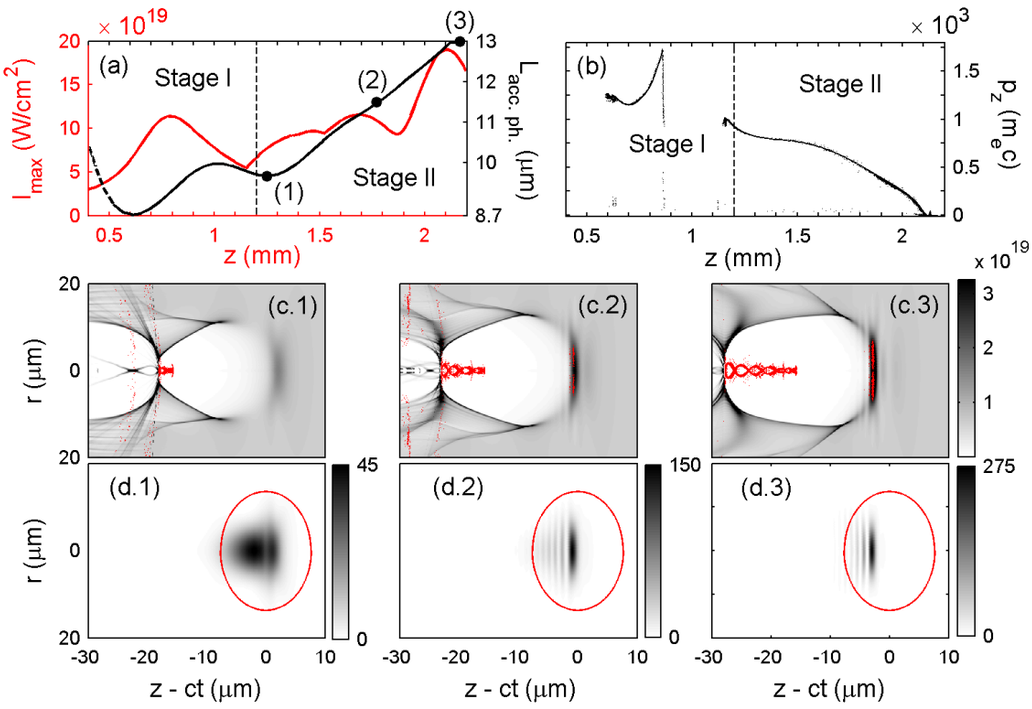

Fig. 5. Pulse self-compression and continuous injection (Kalmykov et al., 2011b). (a) Peak laser intensity (red) and the length of the accelerating phase vs propagation length (black). (b) Energy of test electrons vs their initial positions at $z = 2.2$ mm. The leading quasi-monoenergetic bunch forms during Stage I (one period of bubble size oscillation). Bubble expansion during Stage II causes continuous injection with broad energy spectrum. The bubble and injected test electrons at the positions (1) – (3) of panel (a) are shown in panels (c.1) – (c.3). Grayscale: electron density (in cm^{-3}); red dots: test electrons with $\gamma > \gamma_g$. (d.1) – (d.3) Normalized laser intensity, $|a|^2$, at the positions (1) – (3) of panel (a); red contour: iso-contour of an incident pulse intensity at $\exp(-2)$ of the peak. Self-steepening of the pulse (formation of a relativistic piston) causes elongation of the bubble and continuous injection.

This physical interpretation, deduced from the analysis of quasistatic electron trajectories, is validated in section 2.5 in fully explicit 3-D PIC simulations. It suggests that the root cause of continuous injection is the pulse self-steepening. The steepening is partly caused by depletion due to the wake excitation ($\sim$ 33% at $z = 2.2$ mm) (Decker et al., 1996; Fang et al., 2009; Lu et al., 2007), and is partly a nonlinear optical effect (Faure et al., 2005; Pai et al., 2010; Vieira et al., 2010). Figures 7(a) and 7(b) show axial lineouts of normalized intensity and of the nonlinear index of refraction. The pulse leading edge witnesses the *index down-ramp* at all times. Hence, the laser frequency *red-shifts* in the region of index gradient. At the same time, the tail traveling inside the bubble remains unshifted. With lower frequencies temporally leading higher frequencies, the pulse acquires a *positive chirp*. The anomalous group velocity dispersion of plasma compresses the positively chirped pulse: the red-shifted leading edge slows down with respect to the non-shifted tail, building up the field amplitude first in the pulse head (Fig. 7(a)), and later near the pulse center (Fig. 7(b)). The chirp, as shown in Fig. 7(c), broadens the laser spectrum towards $\omega = \omega_{pe}$; envelope oscillations in Fig. 7(b) result from the strong reduction of the pulse central frequency. The

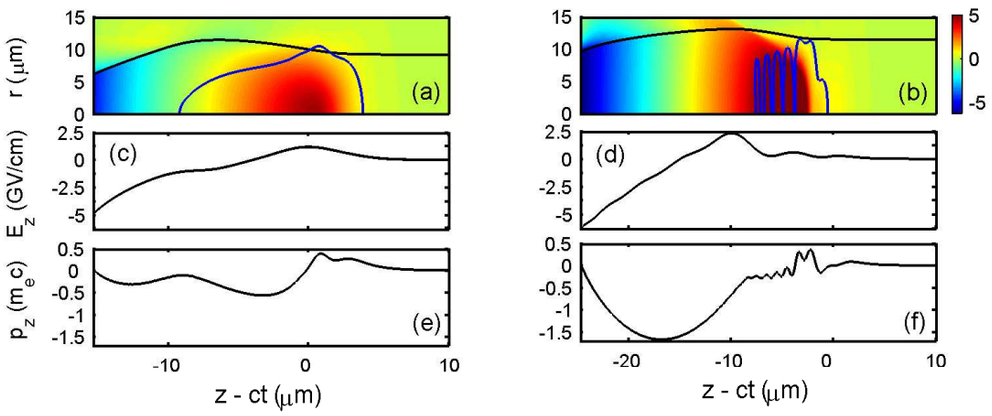

Fig. 6. Bubble elongation due to formation of a relativistic piston: quasistatic analysis. Physical quantities are shown before (left column) and after (right column) the piston formation. The left column corresponds to position (1), and the right column – to the position (3) of Fig. 5(a). (a), (b) Longitudinal electric field E_z (in GV/cm). Black lines are the innermost electron trajectories, $r_{\rm in}(\xi)$, plotted until the point of return, $p_z = 0$. Blue contours are iso-contours of laser intensity at 5×10^{18} W/cm^{-2}. (c), (d) Longitudinal electric field in the points of the innermost electron trajectory, $E_z(r_{\rm in}(\xi))$, from plots (a) and (b), respectively. (e), (f) Longitudinal momentum of the innermost electron along its trajectory, $p_z(r_{\rm in}(\xi))$.

large bandwidth explains pulse compression to roughly two cycles. The red shift of central frequency together with the continuous front etching additionally slows down the pulse and the bubble and provides another reason for the occurrence of continuous injection (Fang et al., 2009). We show in section 3 that *negative chirp* of the incident pulse may compensate for the gradually accumulating red-shift, thus delaying the pulse contraction and partly suppressing continuous injection.

2.5 Validation of self-injection scenarios in full 3-D PIC simulation: role of beam loading

Collective fields of the electron beam, neglected in the test-particle treatment, are known to change the shape of the sheath and thus reduce accelerating gradient, eventually terminating self-injection (Tzoufras et al., 2009). In this section, we verify the test-particle results by running a fully explicit 3-D PIC simulation with the identical set of initial conditions. We use the quasi-cylindrical code CALDER-Circ (Lifschitz et al., 2009), which preserves realistic geometry of interaction, and accounts for the axial asymmetry by decomposing EM fields (laser and wake) into a set of poloidal modes (whereas the particles remain in full 3-D). Well preserved cylindrical symmetry during the interaction enables us to use just the two lowest order modes and thus reduce a 3-D problem to an essentially 2-D one. We suppress sampling noise by using a large number of macroparticles (45 per cell) and high resolution in the direction of propagation, $dz = 0.125c/\omega_0$. The aspect ratio $dr/dz = 15.6$, and the time step $dt = 0.1244\omega_0^{-1}$. Figure 8 shows that despite a much coarser grid, larger time step and underlying approximations, the WAKE simulation correctly captures all relevant physics of plasma wake evolution and dynamics of electron self-injection. In addition, CALDER-Circ having fully self-consistent macroparticle dynamics yields the complete electron phase space, and thus calculates precisely injected charge and beam emittance.

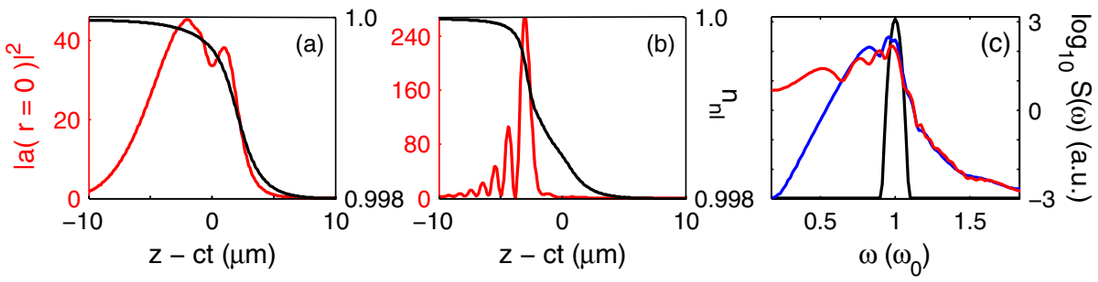

Fig. 7. Pulse red-shifting and formation of the relativistic piston (Kalmykov et al., 2011b). (a) Axial lineouts of normalized intensity (red) and nonlinear refractive index (black) at the position (1) of Fig. 5(a). (b) Same for the position (3) of Fig. 5(a). (c) Laser frequency spectra (radially integrated). Blue corresponds to panel (a), red – to panel (b), black – to the incident pulse. The co-moving index gradient causes frequency red shifting and spectral broadening. The spectrally broadened pulse in panel (b) is compressed to approximately two cycles.

In spite of the great difference in the algorithms and physics content, both codes demonstrate the same correlation between the laser and bubble evolution. Self-injection begins, terminates, and resumes at exactly the same positions along the propagation axis in both runs. Figures 8(a), 8(d), and 8(g) show the result of Stage I — formation of quasi-monoenergetic electron bunch before dephasing. Self-fields of the bunch are unable to prevent the bucket contraction and partial de-trapping of electrons. The bunch phase space has a characteristic "U"-shape produced by the phase space rotation. The bunch has 8% energy spread around 245 MeV and a charge $Q_{\mathrm{mono}} \approx 230$ pC (in addition, electrons from the second bucket produce a separate, rather diffuse peak around 150 MeV in Fig. 8(d)). The bunch duration, $t_b = 10$ fs, is the same as in the test-particle simulation; whereas divergence, 13 mrad, is three times higher. The normalized transverse emittance in the plane of polarization is $\varepsilon_{N,x} = (m_e c)^{-1} \left(\langle \Delta x^2 \rangle \langle \Delta p_x^2 \rangle - \langle \Delta x \Delta p_x \rangle^2 \right)^{1/2} \approx 8.74\pi$ mm mrad. It was understood that the absence of beam self-fields in the test particle model leads to strong underestimation of emittance, which validates the importance of 3-D PIC simulations for precise calculation of the phase space volume of self-injected electrons (Kalmykov et al., 2011b).

The difference between the phase spaces of WAKE test electrons and CALDER-Circ macro-particles, clearly seen in Fig. 8(g), can be attributed to the effect of beam loading which reduces the accelerating gradient along the bunch and slows down phase space rotation, ultimately reducing the bunch energy by 30%. Using the formalism of (Tzoufras et al., 2009), we find that the repulsive EM fields of electron bunch are not high enough to prevent sheath electrons crossing the axis and are thus unable to prevent further injection (Kalmykov et al., 2011b).

Figures 8(a)–8(c) show that continuous injection develops in both CALDER-Circ and WAKE runs in exactly the same fashion, which validates the physical origin and continuous injection scenario inferred from the analysis of quasi-static electron trajectories in section 2.4. Near dephasing, continuously injected charge in CALDER-Circ simulation reaches $Q_{\mathrm{cont}} \approx 1.06$ nC; the beam divergence is 36 mrad. The ratio $Q_{\mathrm{cont}}/Q_{\mathrm{mono}} \approx 4.6$ is lower than the test particle result of section 2.4 on account of beam loading. Figure 8(c) shows that, in spite of the high injected charge, the bubble shape at the dephasing point is almost unaffected by the presence of the electron beam; this observation rules out beam loading as a cause of continuous injection. The bubble is still not fully loaded and injection in the CALDER-Circ simulation continues beyond the dephasing point. Therefore, apart from slight reduction of the accelerating gradient, beam loading brings no new physical features into the scenario of

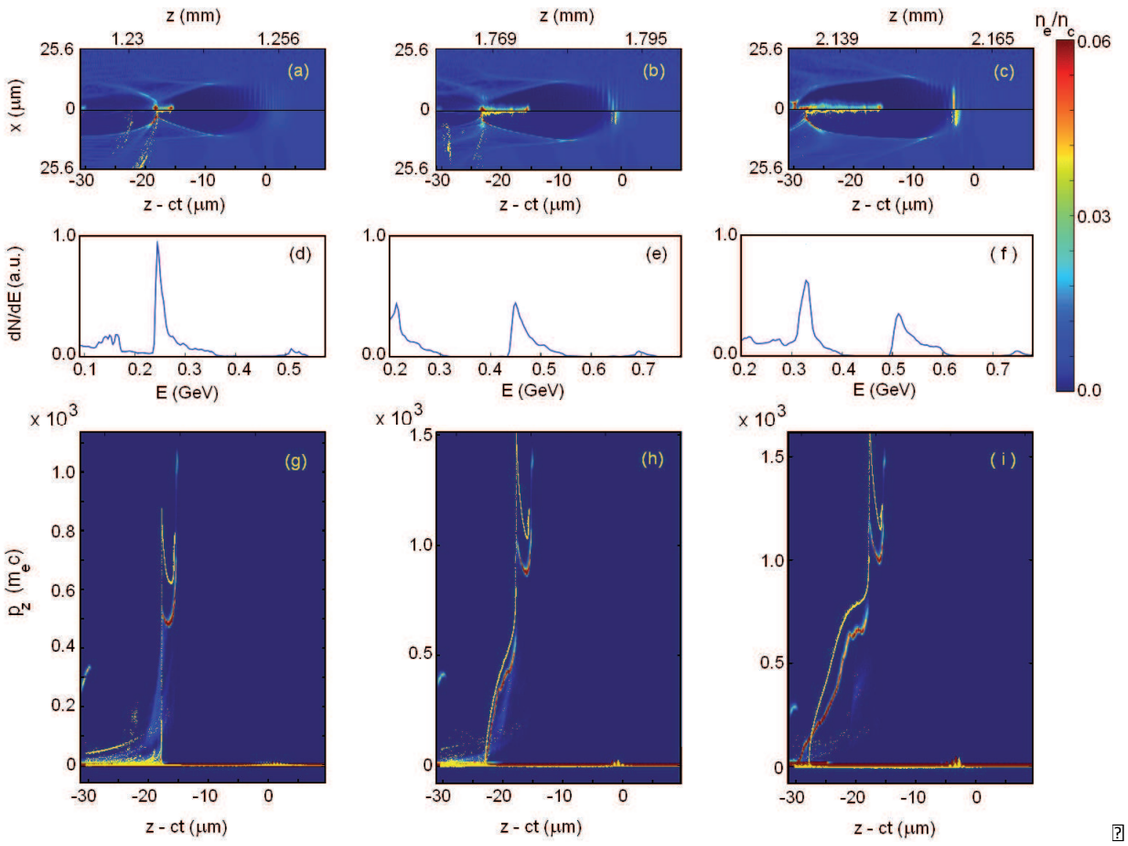

Fig. 8. Continuous injection in quasistatic (WAKE with test particles) and full 3-D PIC (CALDER-Circ) simulations (Kalmykov et al., 2011b). (a)–(c) Electron density from CALDER-Circ (top half) and WAKE (bottom) runs. Yellow dots are the test electrons with $\gamma > \gamma_g$. (d)–(f) Electron energy spectrum (CALDER-Circ). (g)–(i) Longitudinal phase space (colormap – CALDER-Circ; test electrons – yellow dots). Panels (a), (b), (c) are counterparts of Figs. 5(c.1), 5(c.2) and 5(c.3).

continuous injection discussed in section 2.4. Continuous injection can be thus associated solely with frequency red-shift and self-compression of the driver pulse, causing the growth of the quasistatic bubble.

3. Suppression of continuous injection using negatively chirped driving pulse

We have learned in the last section that ploughing through the electron fluid significantly reduces the frequency of the pulse leading edge. Subsequent self-steepening and compression of the driver to a few cycles causes gradual expansion of the bubble, bringing about massive continuous injection, degrading the beam quality. This physical scenario prevents effective use of the entire dephasing length for high-energy quasi-monoenergetic electron acceleration. Using a *negatively chirped* pulse may naturally alleviate this issue. If the pulse has a sufficiently large frequency bandwidth (corresponding to a few-cycle transform-limited duration), the blue shift of the leading edge would largely compensate for a gradually accumulating nonlinear red-shift. This flattening of the phase would then reduce the pulse self-steepening

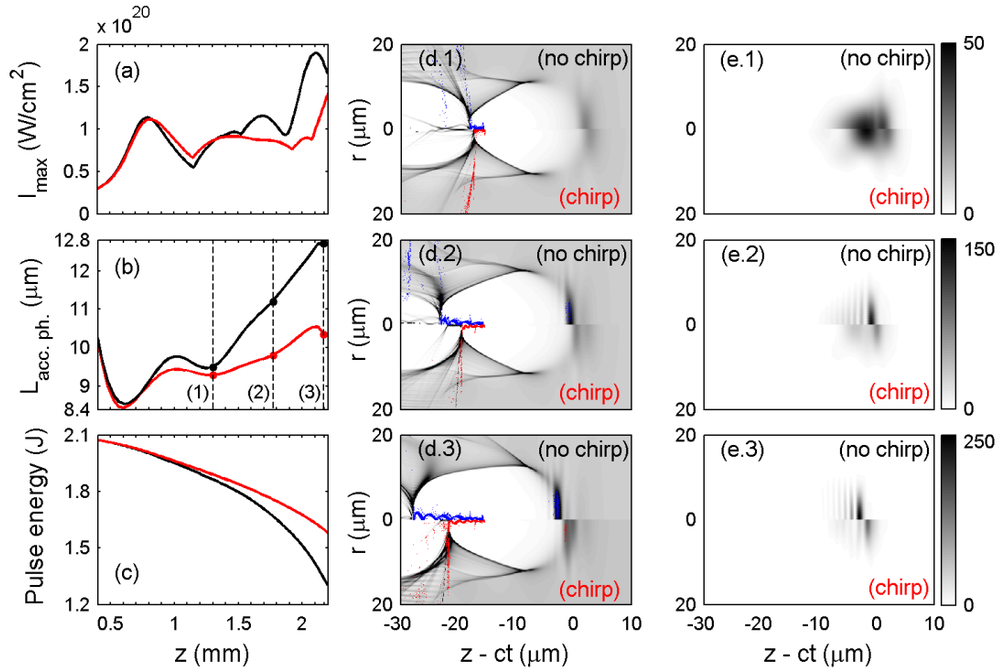

Fig. 9. Effect of the negative chirp on the evolution of driver pulse and plasma bubble. Red lines in panels (a) – (c) correspond to the chirped pulse; black lines to the non-chirped pulse. (a) Peak intensity, (b) length of the accelerating phase, and (c) pulse energy vs propagation distance. Positions (1) – (3) are the same as in Fig. 5(a). Panels (d.1) – (d.3) show electron density and test electrons (red and blue dots) with $\gamma > \gamma_g$ at the positions (1) – (3) (labeled accordingly). Grayscale is linear with a cutoff at $n_e = 3.25 \times 10^{19}$ cm^{-3}. (e.1) – (e.3) Normalized laser intensity, $|a|^2$, at the positions (1) – (3). Negative chirp prevents rapid self-compression of the pulse, slowing down bubble expansion and reducing the number of injected test electrons.

and delay the relativistic piston formation. Elongation of the bubble, vividly demonstrated in Fig. 8, would be thus reduced, and concomitant continuous injection partly suppressed.
We first verify this scenario in a WAKE simulation with test particles. We take the 30 fs, 70 TW Gaussian pulse with the parameters specified at the beginning of section 2 and introduce a linear chirp, temporally advancing higher frequencies. The center of this negatively chirped pulse corresponds to the carrier frequency, and the bandwidth corresponds to a transform-limited 5 fs duration (viz. the relativistic piston of the last section). Multi-Joule amplification systems delivering such broad-bandwidth pulses are not available yet; their development, however, is being actively pursued (Herrmann et al., 2009). As in section 2.4, we run the WAKE simulation until $z = 2.2$ mm. Figures 9 and 10 show that the negative chirp profoundly changes the pulse evolution, and, hence, the dynamics of self-injection.
Figure 9(a) indicates that the initial stage of laser evolution, corresponding to the Stage I of Fig. 5(a), remains almost unaltered. Relativistic self-focusing appears to be quite insensitive to the frequency chirp. Figure 9(b) shows that the bubble experiences one pulsation between $z = 0.6$ and 1.3 mm. The maximal bubble expansion around $z = 1$ mm appears to be 25% smaller than in the non-chirped driver case, with a proportionally smaller number of injected test particles.

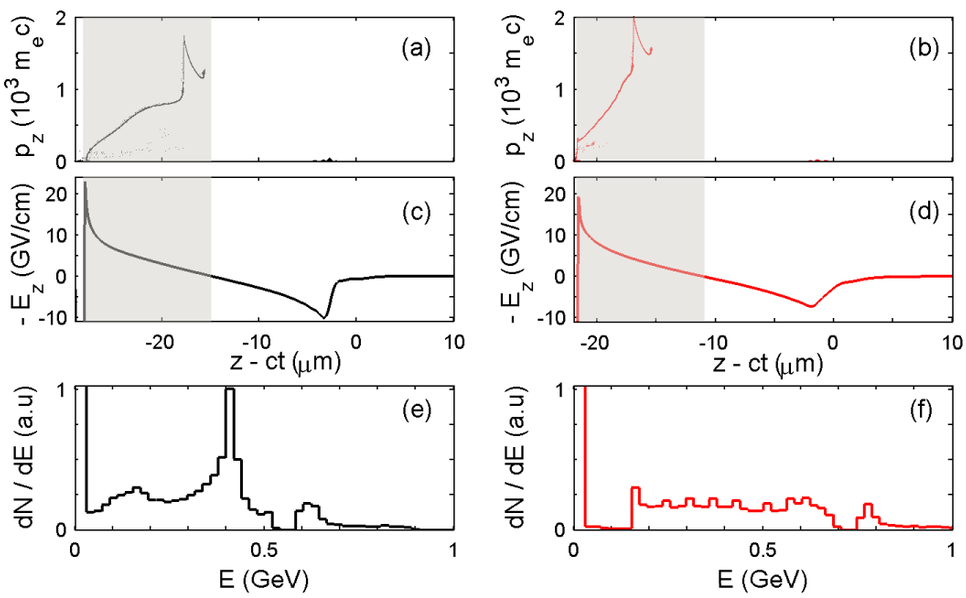

Fig. 10. Reduction of dark current using the negatively chirped driver pulse. Panels on the left correspond to the non-chirped driver, and on the right to the chirped pulse. (a,b) Phase space of test electrons showing signatures of continuous injection. (c,d) Accelerating gradient. Shaded area covers the accelerating phase ($E_z < 0$). (e,f) Energy spectrum of test electrons (number of test particles per spectrometer energy bin). The data are extracted from WAKE simulations at $z = 2.2$ mm (cf. position (3) of Fig. 9(b)). Chirp of the driver reduces expansion of the bubble (cf. panel (d) vs (c)); early dephasing is thus prevented (cf. (b) vs (a)). Injected electrons, exposed to higher accelerating gradient (cf. (d) vs (c)), gain higher energy. The amount of continuously injected charge is significantly reduced (cf. (f) vs (e)).

It is during the Stage II ($z > 1.2$ mm) that the chirp changes the pulse behavior most drastically. From Fig. 9(a), the chirped pulse stabilizes after one spot size oscillation and propagates until $z = 2.1$ mm with almost invariable intensity. As expected, the front steepening remains almost unnoticeable till the end of the run: the chirped pulse envelopes in Figs. 9(e.1) and 9(e.2) show just minimal longitudinal compression. As a result, according to Fig. 9(b), the bubble driven by the chirped pulse expands by roughly 12% between positions (1) and (3), in contrast to 35% in the non-chirped driver case. This stabilizing effect of the pulse chirp is the most vividly seen in progression from Fig. 9(d.1) to 9(d.3).

Figure 9(c) shows 22% depletion of the chirped pulse, in contrast to 33% in the non-chirped driver case. Therefore, the chirped pulse energy is transferred to the plasma wake less effectively. The chirp not only compensates for the nonlinear frequency shift and concomitant pulse self-compression (nonlinear optical effects unrelated to the pump depletion), but also reduces the pulse front etching due to the local pump depletion (Decker et al., 1996). As a result, the chirped pulse propagates with a higher group velocity. The peak of the chirped pulse in Figs. 9(e.1) – 9(e.3) is temporally advanced with respect to its non-chirped counterpart. Larger velocity of the structure extends the dephasing length and, as we shall see below, results in higher final electron energy.

Despite all promising tendencies, continuous injection is not fully shut down. As shown in Figs. 10(a) and 10(b), longitudinal phase space at the end of simulation ($z = 2.2$ mm) consists

	Q_{mono}	E_{mono}	ΔE_{mono}	$\Delta E/E_{\mathrm{mono}}$	$\varepsilon_{N,x}$	$\varepsilon_{N,y}$	$\langle\Delta\alpha\rangle_{\mathrm{mono}}$
Chirp	0.181	637	30	0.047	8.1π	7.4π	10.6
No chirp	0.230	515	44	0.085	8.74π	8.5π	12.9

Table 1. Parameters of the quasi-monoenergetic electron bunch (CALDER-Circ simulation, $z = 2.2$ mm). Q_{mono} is the charge in nC; E_{mono} is the central energy in MeV; ΔE_{mono} is the absolute energy spread (FWHM) in MeV; $\Delta E/E_{\mathrm{mono}}$ is the normalized energy spread; $\varepsilon_{N,x}$ and $\varepsilon_{N,y}$ are the root-mean-square (RMS) normalized transverse emittances (in mm mrad) in and out of the laser polarization plane; $\langle\Delta\alpha\rangle_{\mathrm{mono}}$ is the RMS divergence in mrad.

	Q_{cont}	E_{max}	$\langle\Delta\alpha\rangle_{\mathrm{cont}}$
Chirp	0.46	500	33
No chirp	1.06	400	36

Table 2. Parameters of the low-energy background with continuous spectrum, 50 MeV $< E <$ E_{max} (CALDER-Circ simulation, $z = 2.2$ mm). Q_{cont} is the charge in nC; E_{max} is the high-energy cutoff (in MeV); $\langle\Delta\alpha\rangle_{\mathrm{cont}}$ is the RMS divergence in mrad.

of two distinct components: the leading (quasi-monoenergetic) bunch and long continuous tail. In the non-chirped driver case (cf. Fig. 10(a)), the leading bunch has reached dephasing. In the chirped driver case, however, the electrons are still located deeply inside the accelerating phase and continue gaining energy (cf. Fig. 10(b)). Owing to very slow expansion of the bubble, these particles have been exposed to a higher gradient, gaining additional 150 MeV energy over the same acceleration distance. Comparison of Figs. 10(e) and 10(f) also shows that the dark current is much lower in the chirped driver case, on account of much slower bubble expansion during the second half of the simulation.

We quantify the effect of dark current suppression running a CALDER-Circ simulation with the same initial conditions. We find that the electron beam components – leading quasi-monoenegretic bunch and a polychromatic background – are affected by the pulse chirp differently. Data presented in Tables 1 and 2 show that negative chirp reduces the charge of the background more than twice, and noticeably improves the leading bunch quality, increasing its energy by 20% and reducing the energy spread from 8.5% to 4.7%.

Poor collimation of the continuously injected electrons, $\langle\Delta\alpha\rangle_{\mathrm{cont}} \approx 3\langle\Delta\alpha\rangle_{\mathrm{mono}}$, together with their distribution over the energy range 10-15 times broader than the absolute energy spread of the leading bunch, reduce dramatically the brightness of the energy tail. These poorly collimated beam components can be dispersed in vacuum using miniature magnetic quadrupole lenses, further improving the beam collimation and reducing the energy spread (Weingartner et al., 2011).

More details on electron acceleration in the wake of negatively chirped pulse are shown in Fig. 11. First, comparison of Figs. 11(a.1) and 11(a.2) indicates that the chirped driver can accelerate the leading bunch to a given energy (515 MeV in our case) in a shorter plasma, and with much weaker background. Figures 11(b) also demonstrate that using the negatively chirped driver improves the LPA efficiency, increasing the dephasing length and final electron energy without compromising beam quality. Indeed, Figs. 11(b.2) and 11(b.3) show that, in the chirped driver case, the leading bunch with 181 pC charge, energy 660 MeV and 5.8% relative energy spread remains the dominating spectral feature in the energy range $E > 100$ MeV. In contrast, according to Fig. 11(b.1), electrons accelerated in the wake of non-chirped driver are completely dominated by the dark current by this point.

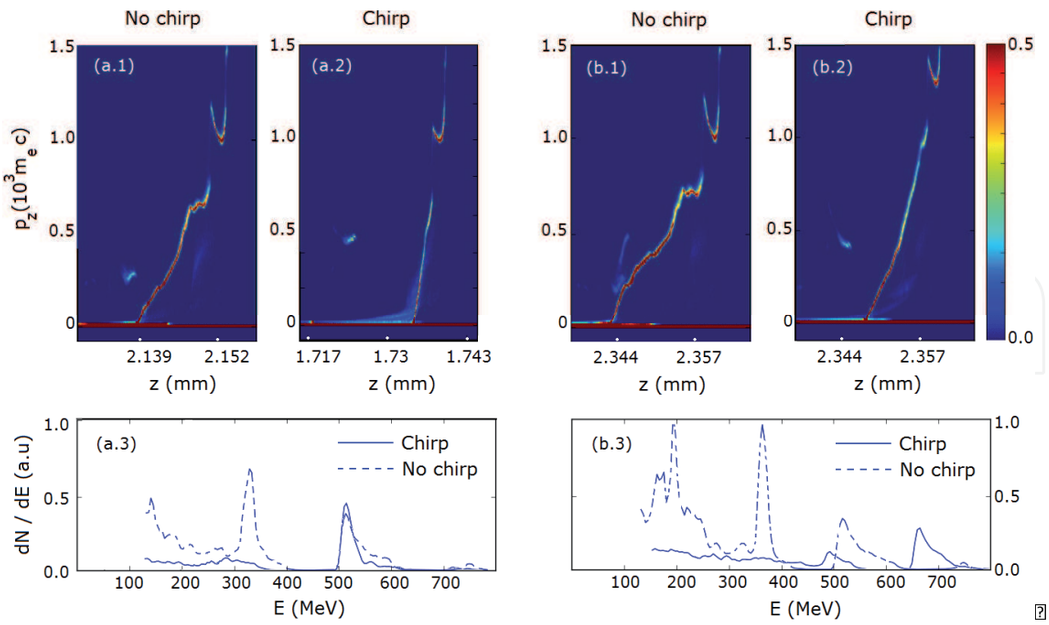

Fig. 11. Acceleration of electrons in the wake of negatively chirped pulse: suppression of dark current (CALDER-Circ simulation). (a.1), (a.2), (b.1), (b.2) Longitudinal phase space; (a.3), (b.3) electron energy spectra. Panel (a.1) – dephasing point of electrons accelerated with the *non-chirped* driver – is the same as Fig. 8(i). The leading bunch with the energy 515 MeV and relative spread 8.5% is followed by a continuous component carrying 4.6 times higher charge. (a.2), (a.3) Electrons accelerated with the chirped driver achieve 515 MeV energy earlier, and with much weaker energy tail. (b.2) Dephasing point of electrons accelerated with the *chirped* driver. Leading bunch with the energy 660 MeV and 5.8% relative spread is the dominating spectral feature in the energy range $E > 100$ MeV (cf. panels (b.2) and (b.3)). At this point, electrons accelerated with the non-chirped pulse are completely dominated by the dark current (cf. panels (b.1) and (b.3)).

In conclusion, 3-D PIC simulations successfully support the idea of suppressing the dark current using negative chirp of the driving pulse. Even though complete elimination of dark current is hard to achieve in high-density plasmas ($\gamma_g = 10 - 15$), strong reduction of the charge in the poorly collimated, continuous low-energy tail is useful for applications. Subsequent manipulations with the beam using permanent magnets may further improve its quality (Weingartner et al., 2011).

4. Conclusion

A time-varying electron density bubble created by the radiation pressure of a tightly focused laser pulse guides the pulse through a uniform, rarefied plasma, traps ambient plasma electrons and accelerates them to GeV-level energy. Natural pulse evolution (nonlinear focusing and self-compression) *is in most cases sufficient* to initiate and terminate self-injection. Bubble dynamics and the self-injection process are governed primarily by the driver evolution. Expansion of the bubble facilitates injection, whereas stabilization and contraction extinguishes injection and suppresses the low-energy background. Simultaneously, longitudinal non-uniformity of the accelerating gradient causes rapid phase space rotation.

Although beam loading reduces the accelerating gradient and slows down phase space rotation, a quasi-monoenergetic, well collimated electron bunch forms long before dephasing. At the same time, extending the acceleration length to the dephasing limit without compromising electron beam quality is not straightforward. In modern experiments, phase self-modulation and frequency red-shift due to the wake excitation cause gradual compression of the driver pulse, turning it into a relativistic piston. This process causes bubble elongation and massive continuous secondary injection (dark current). Compensation of the nonlinear frequency shift by negatively chirping the pulse is one way to delay the piston formation. As a result, nearly 60% reduction of the dark current is observed in our 3-D PIC simulations. The same set of simulations also shows that higher stability of the broad bandwidth negatively chirped pulse in plasma leads to a 20% increase in the central energy, a 50% reduction of relative energy spread, and a 20% emittance reduction of the quasi-monoenergetic, high-energy component of electron beam.

The reported results highlight the importance of reduced physics models. Reduced models not only lower the the computational cost of simulations (sometimes by many orders of magnitude), but also allow for the identification of the underlying physical processes responsible for the observed phenomena. The self-injection dynamics and its relation to the nonlinear optical evolution of the driver was understood using especially simple simulation tools (cylindrical quasistatic PIC code with fully 3-D dynamic test particle module). In practical terms, this means that the system performance (electron beam duration, mean energy, energy spread, and, very roughly, divergence) can be approximately assessed without recourse to computationally intensive 3-D PIC simulations. It appears, however, that calculation of the beam charge and transverse emittance still needs a 3-D fully kinetic simulation. Clarifying the nature of self-consistent effects affecting the phase space volume of self-injected electrons in various numerical models, and establishing the true physical origin of these effects is the subject of ongoing work.

5. Acknowledgements

S. Y. K. is grateful to S. A. Yi, V. Khudik, and M. C. Downer for many stimulating discussions and keen interest in the work presented in this Chapter. The work is partly supported by the U. S. Department of Energy grant DE-FG02-08ER55000. A. B. and E. L. acknowledge the support of LASERLAB-EUROPE/LAPTECH through EC FP7 contract no. 228334. The authors acknowledge CCRT at CEA (www-ccrt.cea.fr) for providing computing resources.

6. References

Andreev, N. E., Gorbunov, L. M., Mora,. P & Ramazashvili, R. R. (2007). Filamentation of ultrashort laser pulses propagating in tenuous plasmas, *Phys. Plasmas* 14(8): 083104.

Aoyama, M., Yamakawa, K., Akahane, Y., Ma, J., Inoue, N., Ueda, H. & Kiriyama, H. (2003). 0.85-PW, 33-fs Ti:sapphire laser, *Opt. Lett.* 28(17): 1594–1596.

Brozek-Pluska, B., Gliger, D., Hallou, A., Malka, V. & Gauduel, Y. A. (2005). Direct observation of elementary radical events: low- and high-energy radiation femtochemistry in solutions, *Radiat. Phys. Chem.* 72: 149–157.

Brunetti, E., Shanks, R. P., Manahan, G. G., Islam, M. R., Ersfeld, B., Anania, M. P., Cipiccia, S., Issac, R. C., Raj, G., Vieux, G., Welsh, G., H., Wiggins, S. M. & Jaroszynski, D. A. (2010). Low emittance, high brilliance relativistic electron beams from a laser-plasma accelerator, *Phys. Rev. Lett.* 105(21): 215007.

Buck, A., Nicolai, M., Schmid, K., Sears, C. M. S., Sävert, A., Mikhailova, J. M., Krausz, F., Kaluza, M. C. & Veisz, L. (2011). Real-time observation of laser-driven electron acceleration, *Nature Phys.* 7: 543–548.

Clayton, C. E., Ralph, J. E., Albert, F., Fonseca, R. A., Glenzer, S. H., Joshi, C., Lu, W., Marsh, K. A., Martins, S. F., Mori, W. B., Pak, A., Tsung, F. S., Pollock, B. B., Ross, J. S., Silva, L. O. & Froula, D. H. (2010). Self-guided laser wakefield acceleration beyond 1 GeV using ionization-induced injection, *Phys. Rev. Lett.* 105(10): 105003.

DesRosiers, C., Moskvin, V., Bielajew, A. F. & Papiez, L. (2000). 150-250 meV electron beams in radiation therapy, *Phys. Med. Biol.* 45(7): 1781–1805.

Dong, P., Reed, S. A., Yi, S. A., Kalmykov, S., Shvets, G., Downer, M. C., Matlis, N. H., Leemans W. P., McGuffey, C., Bulanov, S. S., Chvykov, V., Kalintchenko, G., Krushelnick, K., Maksimchuk, A., Matsuoka, T., Thomas, A. G. R. & Yanovsky, V. (2010a). Formation of optical bullets in laser-driven plasma bubble accelerators, *Phys. Rev. Lett.* 104(13): 134801.

Dong, P., Reed, S. A., Yi, S. A., Kalmykov, S., Li, Z. Y., Shvets, G., Matlis, N. H., McGuffey, C., Bulanov, S. S., Chvykov, V., Kalintchenko, G., Krushelnick, K., Maksimchuk, A., Matsuoka, T., Thomas, A. G. R., Yanovsky, V. & Downer, M. C. (2010b). Holographic visualization of laser wakefields, *New J. Phys.* 12(4): 045016.

Decker, C. D., Mori, W. B., Tzeng, K.-C. & Katsouleas, T. (1996). The evolution of ultra-intense, short-pulse lasers in underdense plasmas, *Phys. Plasmas* 3(5): 2047–2056.

Esarey, E., Schroeder, C. B. & Leemans, W. P. (2009). Physics of laser-driven plasma-based electron accelerators, *Rev. Mod. Phys.* 81(3): 1229–1285.

Fang, F., Clayton, C. E., Marsh, K. A., Pak, A. E., Ralph, J. E., Lopes, N. C. & Joshi, C. (2009). Pump depletion limited evolution of the relativistic plasma wave-front in a forced laser-wakefield accelerator, *Plasma Phys. Control. Fusion* 51: 024003.

Faure, J., Glinec, Y., Santos, J. J., Ewald, F., Rousseau, J.-P., Kiselev, S., Pukhov, A., Hosokai, T. & Malka. V. (2005). Observation of laser-pulse shortening in nonlinear plasma waves, *Phys. Rev. Lett.* 95(20): 205003.

Faure, J., Glinec, Y., Gallot, G. & Malka, V. (2006). Ultrashort laser pulses and ultrashort electron bunches generated in relativistic laser-plasma interaction, *Phys. Plasmas* 13(5): 056706.

Froula, D. H., Clayton, C. E., Döppner, T., Marsh, K. A., Barty, C. P. J., Divol, L., Fonseca, R. A., Glenzer, S. H., Joshi, C., Lu, W., Martins, S. F., Michel, P., Mori, W. B., Palastro, J. P., Pollock, B. B., Pak, A., Ralph, J. E., Ross, J. S., Siders, C. W., Silva, L. O. & Wang T. (2009). Measurements of the critical power for self-injection of electrons in a laser wakefield accelerator, *Phys. Rev. Lett.* 103(21): 215006.

Fuchs, M., Weingartner, R., Popp, A., Major, Zs., Becker, S., Osterhoff, J., Cortrie, I., Zeitler, B., Hörlein, R., Tsakiris, G. D., Schramm, U., Rowlands-Rees, T. P., Hooker, S. M., Habs, D., Krausz, F., Karsch, S. & Grüner, F. (2009). Laser-driven soft-X-ray undulator source, *Nature Phys.* 5: 826–829.

Gaul, E. W., Martinez, M., Blakeney, J., Jochmann, A., Ringuette, M., Hammond, D., Borger, T., Escamilla, R., Douglas, S., Henderson, W., Dyer, G., Erlandson, A., Cross, R., Caird, J., Ebbers, C. & Ditmire., T. (2010). Demonstration of a 1.1 petawatt laser based on a hybrid optical parametric chirped pulse amplification/mixed Nd:glass amplifier *Appl. Opt.* 49(9): 1676–1681.

Glinec, Y., Faure, J., Le Dain, L., Darbon, S., Hosokai, T., Santos, J. J., Lefebvre, E., Rousseau, J. P., Burgy, F., Mercier, B. & Malka, V. (2005). High-resolution γ-ray radiography produced by a laser-plasma driven electron source, *Phys. Rev. Lett.* 94(2): 025003.

Glinec, Y., Faure, J., Malka, V., Fuchs, T., Szymanowski, H. & Oelfke, U. (2006). Radiotherapy with laser-plasma accelerators: Monte Carlo simulation of dose deposited by an experimental quasimonoenergetic electron beam, *Med. Phys.* 33(1): 155–162.

Gorbunov, L. M., Kalmykov, S. Yu. & Mora, P. (2005). Laser wakefield acceleration by petawatt ultrashort laser pulses, *Phys. Plasmas* 12(3): 033101.

Gordienko, S. & Pukhov. A. (2005). Scalings for ultrarelativistic laser plasmas and quasimonoenergetic electrons, *Phys. Plasmas* 12(4): 043109.

Gordon, D. F., Ting, A., Helle, M. H., Kaganovich, D. & Hafizi, B. (2010). Electro-optic shocks from blowout laser wakefields, *New J. Phys.* 12(4): 045026.

Grüner, F., Becker, S., Schramm, U., Eichner, T., Fuchs, M., Weingartner, R., Habs, D., Meyer-ter-Vehn, J., Geissler, M., Ferrario, M., Serafini, L., van der Geer, B., Backe, H., Lauth, W. & Reiche, S. (2007). Design considerations for table-top, laser-based VUV and X-ray free electron lasers, *Appl. Phys. B: Lasers Opt.* 86: 431–435.

Hafizi, B., Ting, A., Sprangle, P. & Hubbard, R. F. (2000). Relativistic focusing and ponderomotive channeling of intense laser beams, *Phys. Rev. E* 62(3): 4120–4125.

Hafz, N. A. M., Jeong, T. M., Choi, I., Lee, S. K., Pae, K. H., Kulagin, V. V., Sung, J. H., Yu, T. J., Hong, K.-H., Hosokai, T., Cary, J. R., Ko, D.-K. & Lee, J. (2008). Stable generation of GeV-class electron beams from self-guided laser-plasma channels, *Nat. Photon.* 2: 571–577.

Hafz, N. A. M., Lee, S. K., Jeong, T. M. & Lee, J. (2011). Evolution of self-injected quasi-monoenergetic electron beams in a plasma bubble, *Nucl. Instrum. Methods in Phys. Res. A* 637: S51–S53.

Hartemann, F. V., Gibson, D. J., Brown, W. J., Rousse, A., Ta Phuoc, K., Malka, V., Faure, J. & Pukhov, A. (2007). Compton scattering x-ray sources driven by laser wakefield acceleration, *Phys. Rev. ST Accel. Beams* 10(1): 011301.

Hein, J., Kaluza, M. C., Bödefeld, R., Siebold, M., Podleska, S. & Sauerbrey, R. (2006). POLARIS: an all diode-pumped ultrahigh peak power laser for high repetition rates, *Lect. Notes Phys.* 694: 47–66.

Helle, M. H., Kaganovich, D., Gordon, D. F. & Ting, A. (2010). Measurement of electro-optic shock and electron acceleration in a strongly cavitated laser wakefield accelerator, *Phys. Rev. Lett.* 105(10): 105001.

Hemker, R. G., Hafz, N. M. & Uesaka, M. (2002). Computer simulations of a single-laser double-gas-jet wakefield accelerator concept, *Phys. Rev. ST Accel. Beams* 5(4): 041301.

Herrmann, D., Veisz, L., Tautz, R., Tavella, F., Schmid, K., Pervak, V. & and Krausz, F. (2009). Generation of sub-three-cycle, 16 TW light pulses by using noncollinear optical parametric chirped-pulse amplification, *Opt. Lett.* 34(16): 2459-2461.

Hidding, B., Königstein, T., Willi, O., Rosenzweig, J. B., Nakajima, K. & Pretzler, G. (2011). Laser-plasma-accelerators – a novel, versatile tool for space radiation studies, *Nucl. Instrum. Methods in Phys. Res. A* 636: 31–40.

Kaganovich, D., Gordon, D. F. & Ting, A. (2008). Observation of large-angle quasi-monoenergetic electrons from a laser wakefield, *Phys. Rev. Lett.* 100(21): 215002.

Kainz, K. K., Hogstrom, K. R., Antolak, J. A., Almond, P. R., Bloch, C. D., Chiu, C., Fomytskyi, M., Raischel, F., Downer, M. & Tajima, T. (2004). Dose properties of a laser accelerated electron beam and prospects for clinical application, *Med. Phys.* 31(7): 2053–2067.

Kalmykov, S., Yi, S. A., Khudik, V. & Shvets, G. (2009). Electron self-injection and trapping into an evolving plasma bubble, *Phys. Rev. Lett.* 103(13): 135004.

Kalmykov, S. Y., Yi, S. A., Beck, A., Lifschitz, A. F., Davoine, X., Lefebvre, E., Pukhov, A., Khudik, V., Shvets, G., Reed, S. A., Dong, P., Wang, X., Du, D., Bedacht, S.,

Zgadzaj, R., Henderson, W., Bernstein, A., Dyer, G., Martinez, M., Gaul, E., Ditmire, T. & Downer, M. C. (2010a). Numerical modelling of a 10-cm-long multi-GeV laser wakefield accelerator driven by a self-guided petawatt pulse, *New J. Phys.* 12(4): 045019.

Kalmykov, S. Y., Beck, A., Yi, S. A., Khudik, V., Shadwick, B. A., Lefebvre, E. & Downer, M. C. (2010b). Electron self-injection into an evolving plasma bubble: the way to a dark current free GeV-scale laser accelerator, *AIP Conf. Proc.* 1299: 174–179.

Kalmykov, S. Y., Yi, S. A., Beck, A., Lifschitz, A. F., Davoine, X., Lefebvre, E., Khudik, V., Shvets, G. & Downer, M. C. (2011a). Dark-current-free petawatt laser-driven wakefield accelerator based on electron self-injection into an expanding plasma bubble, *Plasma Phys. Control. Fusion* 53: 014006.

Kalmykov, S. Y., Beck, A., Yi, S. A., Khudik, V. N., Downer, M. C., Lefebvre, E., Shadwick, B. A. & Umstadter, D. P. (2011b). Electron self-injection into an evolving plasma bubble: quasi-monoenergetic laser-plasma acceleration in the blowout regime, *Phys. Plasmas* 18(5): 056704.

Kneip, S., Nagel, S. R., Martins, S. F., Mangles, S. P. D., Bellei, C., Chekhlov, O., Clarke, R. J., Delerue, N., Divall, E. J., Doucas, G., Ertel, K., Fiúza, F., Fonseca, R., Foster, P., Hawkes, S. J., Hooker, C. J., Krushelnick, K., Mori, W. B., Palmer, C. A. J., Ta Phuoc, K., Rajeev, P. P., Schreiber, J., Streeter, M. J. V., Urner, D., Vieira, J., Silva, L. O. & Najmudin Z. (2009). Near-GeV acceleration of electrons by a nonlinear plasma wave driven by a self-guided laser pulse, *Phys. Rev. Lett.* 103(3): 035002.

Kneip, S., McGuffey, C., Martins, J. L., Martins, S. F., Bellei, C., Chvykov, V., Dollar, F., Fonseca, R., Huntington, C., Kalintchenko, G., Maksimchuk, A., Mangles, S. P. D., Matsuoka, T., Nagel, S. R., Palmer, C. A. J., Schreiber, J., Ta Phuoc, K., Thomas, A. G. R., Yanovsky, V., Silva, L. O., Krushelnick K. & Najmudin Z. (2010). Bright spatially coherent synchrotron X-rays from a table-top source, *Nature Phys.* 6: 980–983.

Korzhimanov, A. V., Gonoskov, A. A., Khazanov, E. A., & Sergeev A. M. (2011). Horizons of petawatt laser technology, *Physics – Uspekhi* 54(1): 9–28.

Kostyukov, I., Nerush, E., Pukhov, A. & Seredov., V. (2009). Electron self-injection in multidimensional relativistic-plasma wake fields, *Phys. Rev. Lett.* 103(17): 175003.

Leemans, W. P., Rodgers, D., Catravas, P. E., Geddes, C. G. R., Fubiani, G., Esarey, E., Shadwick, B. A., Donahue, R. & Smith, A. (2001). Gamma-neutron activation experiments using laser wakefield accelerators, *Phys. Plasmas* 8(5): 2510–2516.

Leemans, W. P., Nagler, B., Gonsalves, A. J., Tóth, Cs., Nakamura, K., Geddes, C. G. R., Esarey, E., Schroeder, C. B. & Hooker S. M. (2006). GeV electron beams from a centimetre-scale accelerator, *Nature Phys.* 2: 696–699.

Li, Z., Zgadzaj, R., Wang, X., Reed, S., Dong, P. & Downer, M. C. (2010). Frequency-domain streak camera for ultrafast imaging of evolving light-velocity objects, *Opt. Lett.* 35(24): 4087–4089.

Li, Z., Zgadzaj, R., Wang, X., Dong, P. & Downer, M. C. (2011). Frequency-domain tomography of evolving light-velocity objects, in *Quantum Electronics and Laser Science Conference*, Baltimore, Maryland, OSA Technical Digest (CD) (Optical Society of America, 2011), paper QTuB2; *www.opticsinfobase.org/abstract.cfm?URI=QELS-2011-QTuB2*

Lifschitz, A. F., Davoine, X., Lefebvre, E., Faure, J., Rechatin, C. & Malka, V (2009). Particle-in-Cell modelling of laser-plasma interaction using Fourier decomposition, *J. Comput. Phys.* 228: 1803–1814.

Liu, J. S., Xia, C. Q., Wang, W. T., Lu, H. Y., Wang, Ch., Deng, A. H., Li, W. T., Zhang, H., Liang, X. Y., Leng, Y. X., Lu, X. M., Wang, C., Wang, J. Z., Nakajima, K., Li, R. X & Xu, Z.

Z. (2011). All-optical cascaded laser wakefield accelerator using ionization-induced injection, *Phys. Rev. Lett.* 107(3): 035001.

Lu, W., Huang, C., Zhou, M., Tzoufras, M., Tsung F. S., Mori, W. B. & Katsouleas, T. (2006). A nonlinear theory for multidimensional relativistic plasma wave wakefields, *Phys. Plasmas* 13(5): 056709.

Lu, W., Tzoufras, M., Joshi, C., Tsung, F. S., Mori, W. B., Vieira, J., Fonseca, R. A. & Silva, L. O. (2007). Generating multi-GeV electron bunches using single stage laser wakefield acceleration in a 3D nonlinear regime, *Phys. Rev. ST Accel. Beams* 10(6): 061301.

Lundh, O., Lim, J., Rechatin, C., Ammoura, L., Ben-Ismail, A., Davoine, X., Gallot, G., Goddet, J.-P., Lefebvre, E., Malka, V. & Faure, J. (2011). Few femtosecond, few kiloampere electron bunch produced by a laser-plasma accelerator, *Nature Phys.* 7: 219–222.

Maksimchuk, A., Reed, S., Naumova, N., Chvykov, V., Hou, B., Kalintchenko, G., Matsuoka, T., Nees, J., Rousseau, P., Mourou, G., Yanovsky, V. (2007). Energy scaling of quasi-monoenergetic electron beams from laser wakefields driven by 40-TW ultra-short pulses, *Appl. Phys B: Lasers Opt.* 89: 201–207.

Malka, V., Faure, J., Marquès, J. R., Amiranoff, F., Rousseau, J. P., Ranc, S., Chambaret, J. P., Najmudin, Z., Walton, B., Mora, P. & Solodov, A. (2001). Characterization of electron beams produced by ultrashort (30 fs) laser pulses, *Phys. Plasmas* 8(6): 2605–2608.

Malka, V., Faure, J., Rechatin, C., Ben-Ismail, A., Lim, J. K., Davoine, X. & Lefebvre, E. (2009). Laser-driven accelerators by colliding pulses injection: A review of simulation and experimental results, *Phys. Plasmas* 16(5): 056703.

Malka, V., Faure, J. & Gauduel, Y. A. (2010). Ultra-short electron beams based spatio-temporal radiation biology and radiotherapy, *Mutat. Res.: Rev. Mutat. Res.* 704(1-3): 145–151.

Mangles, S. P. D., Thomas, A. G. R., Lundh, O., Lindau, F., Kaluza, M. C., Persson, A., Wahlström, C.-G., Krushelnick, K. & Najmudin, Z. (2007). On the stability of laser wakefield electron accelerators in the monoenergetic regime, *Phys. Plasmas* 14(5): 056702.

Martins, S. F., Fonseca, R. A., Lu, W., Mori, W. B. & Silva L. O. (2010). Exploring laser-wakefield-accelerator regimes for near-term lasers using particle-in-cell simulation in Lorentz-boosted frames, *Nature Phys.* 6: 311–316.

Mora, P. & Antonsen Jr., T. M. (1996). Electron cavitation and acceleration in the wake of an ultraintense, self-focused laser pulse, *Phys. Rev. E* 53(3): R2068–R2071.

Mora, P. & Antonsen Jr., T. M. (1997). Kinetic modeling of intense, short laser pulses propagating in tenuous plasmas, *Phys. Plasmas* 4(1): 217–229.

Morshed, S., Antonsen, Jr., T. M. & Palastro, J. P. (2010). Efficient simulation of electron trapping in laser and plasma wakefield acceleration, *Phys. Plasmas* 17(6): 063106.

Mourou, G. A., Tajima, T. & Bulanov, S. V. (2006). Optics in the relativistic regime, *Rev. Mod. Phys.* 78(2): 309–371.

Oguchi, A., Zhidkov, A., Takano, K., Hotta, E., Nemoto, K. & Nakajima, K. (2008). Multiple self-injection in the acceleration of monoenergetic electrons by a laser wake field, *Phys. Plasmas* 15(4): 043102.

Osterhoff, J., Popp, A., Major, Zs., Marx, B., Rowlands-Rees, T. P., Fuchs, M., Geissler, M., Hörlein, R., Hidding, B., Becker, S., Peralta, E. A., Schramm, U., Grüner, F., Habs, D., Krausz, F., Hooker, S. M. & Karsch, S. (2008). Generation of stable, low-divergence electron beams by laser-wakefield acceleration in a steady-state-flow gas cell, *Phys. Rev. Lett.* 101(8): 085002.

Pai, C.-H., Chang, Y.-Y., Ha, L.-C., Xie, Z.-H., Lin, M.-W., Lin, J.-M., Chen, Y.-M., Tsaur, G., Chu, H.-H., Chen, S.-H., Lin, J.-Y., Wang, J. & Chen, S.-Y. (2010). Generation of intense

ultrashort midinfrared pulses by laser-plasma interaction in the bubble regime, *Phys. Rev. A* 82(6): 063804.

Pukhov, A. & Meyer-ter-Vehn, J. (2002). Laser wake field acceleration: the highly non-linear broken-wave regime, *Appl. Phys. B: Lasers Opt.* 74: 355–361.

Pukhov, A., an der Brügge, D. & Kostyukov, I. (2010). Relativistic laser plasmas for electron acceleration and short wavelength radiation generation, *Plasma Phys. Control. Fusion* 52: 124039.

Quesnel, B. & Mora, P. (1998). Theory and simulation of the interaction of ultraintense laser pulses with electrons in vacuum, *Phys. Rev. E* 58(3): 3719–3732.

Ralph, J. E., Marsh, K. A., Pak, A. E., Lu, W., Clayton, C. E., Fang, F., Mori, W. B. & and Joshi, C. (2009). Self-guiding of ultrashort, relativistically intense laser pulses through underdense plasmas in the blowout regime, *Phys. Rev. Lett.* 102(17): 175003.

Ramanathan, V., Banerjee, S., Powers, N., Cunningham, N., Chandler-Smith, N. A., Zhao, K., Brown, K., Umstadter, D., Clarke, S., Pozzi, S., Beene, J., Vane, C. R. & Schultz, D. (2010). Submillimeter-resolution radiography of shielded structures with laser-accelerated electron beams, *Phys. Rev. ST Accel. Beams* 13(10): 104701.

Rechatin, C., Faure, J., Davoine, X., Lundh, O., Lim, J., Ben-Ismail, A., Burgy, F., Tafzi, A., Lifschitz, A. F., Lefebvre, E. & Malka, V. (2010). Characterization of the beam loading effects in a laser plasma accelerator, *New J. Phys.* 12(4): 045023.

Reed, S. A., Chvykov, V., Kalintchenko, G., Matsuoka, T., Yanovsky, V., Vane, C. R., Beene, J. R., Stracener, D., Schultz, D. R. & Maksimchuk, A. (2007). Efficient initiation of photonuclear reactions using quasimonoenergetic electron beams from laser wakefield acceleration, *J. Appl. Phys.* 102(7): 073103.

Rosenzweig, J. B., Breizman, B., Katsouleas, T. & Su, J. J. (1991). Acceleration and focusing of electrons in two-dimensional nonlinear plasma wake fields, *Phys. Rev. A* 44(10): R6189–R6192.

Ross, I. N., Collier, J. L., Matousek, P., Danson, C. N., Neely, D., Allott, R. M., Pepler, D. A., Hernandez-Gomez, C. & Osvay, K. (2000). Generation of terawatt pulses by use of optical parametric chirped pulse amplification, *Appl. Opt.* 39(15): 2422–2427.

Rousse, A., Ta Phuoc, K., Shah, R., Fitour, R. & Albert, F. (2007). Scaling of betatron X-ray radiation, *Eur. Phys. J. D* 45: 391–398.

Schlenvoigt, H.-P., Haupt, K., Debus A., Budde, F., Jäckel, O., Pfotenhauer, S., Schwoerer, H., Rohwer, E., Gallacher, J. G., Brunetti, E., Shanks, R. P., Wiggins, S. M. & Jaroszynski, D. A. (2008). A compact synchrotron radiation source driven by a laser-plasma wakefield accelerator, *Nature Phys.* 4: 130–133.

Schroeder, C. B., Esarey, E., Geddes, C. G. R., Benedetti, C. & Leemans, W. P. (2010). Physics considerations for laser-plasma linear colliders, *Phys. Rev. ST Accel. Beams* 1310: 101301.

Sun, G.-Z., Ott, E., Lee, Y. C. & Guzdar, P. (1987). Self-focusing of short intense pulses in plasmas, *Phys. Fluids* 30(2): 526–532.

Semushin, S. & Malka, V. (2001). High density gas jet nozzle design for laser target production, *Rev. Sci. Instrum.* 72(7): 2961–2965.

Spence, D. J. & Hooker, S. M. (2001). Investigation of a hydrogen plasma waveguide, *Phys. Rev. E* 63(1): 015401(R).

Spence, D. E., Kean, P. N. & Sibbett, W. (1991) 60-fsec pulse generation from a self-mode-locked Ti:sapphire laser, *Opt. Lett.* 16(1): 42–44.

Strickland, D. & Mourou, G. (1985). Compression of amplified chirped optical pulses, *Opt. Commun.* 56(3): 219–221.

Suk, H., Barov, N., Rosenzweig, J. B. & Esarey, E. (2001). Plasma electron trapping and acceleration in a plasma wake field using a density transition, *Phys. Rev. Lett.* 86(6): 1011–1014.

Sung, J. H., Lee, S. K., Yu, T. J., Jeong, T. M. & Lee, J. (2010). 0.1 Hz 1.0 PW Ti:sapphire laser, *Opt. Lett.* 35(18): 3021–3023.

Tajima, T. & Dawson, J. M. (1979). Laser electron accelerator, *Phys. Rev. Lett.* 43(4): 267–270.

Thomas, A. G. R., Mangles, S. P. D., Najmudin, Z., Kaluza, M. C., Murphy, C. D. & Krushelnick, K. (2007) Measurements of wave-breaking radiation from a laser-wakefield accelerator, *Phys. Rev. Lett.* 98(5): 054802.

Thomas, A. G. R., Najmudin, Z., Mangles, S. P. D., Murphy, C. D., Dangor, A. E., Kamperidis, C., Lancaster, K. L., Mori, W. B., Norreys, P. A., Rozmus, W. & Krushelnick, K. (2007). The effect of laser focusing conditions on propagation and monoenergetic electron production in laser wakefield accelerators, *Phys. Rev. Lett.* 98(9): 095004.

Thomas, A. G. R., Mangles, S. P. D., Murphy, C. D., Dangor, A. E., Foster, P. S., Gallacher, J. G., Jaroszynski, D. A., Kamperidis, C., Krushelnick, K., Lancaster, K. L., Norreys, P. A., Viskup, R. & Najmudin, Z. (2009). Ultrashort pulse filamentation and monoenergetic electron beam production in LWFAs, *Plasma Phys. Control. Fusion* 51: 024010.

Tsung, F. S., Lu, W., Tzoufras, M., Mori, W. B., Joshi, C., Vieira, J. M., Silva, L. O. & Fonseca, R. A. (2006). Simulation of monoenergetic electron generation via laser wakefield accelerators for 5-25 TW lasers, *Phys. Plasmas* 13(5): 056708.

Tzoufras, M., Lu, W., Tsung, F. S., Huang, C., Mori, W. B., Katsouleas, T., Vieira, J., Fonseca, R. A. & Silva, L. O. (2009). Beam loading by electrons in nonlinear plasma wake, *Phys. Plasmas* 16(5): 056705.

Vieira, J., Fiúza, F., Silva, L. O., Tzoufras, M. & Mori W. B. (2010). Onset of self-steepening of intense laser pulses in plasmas, *New J. Phys.* 12(4): 045025.

Weingartner, R., Fuchs, M., Popp, A., Raith, S., Becker, S., Chou, S., Heigoldt, M., Khrennikov, K., Wenz, J., Seggebrock, T., Zeitler, B., Major, Zs., Osterhoff, J., Krausz, F., Karsch, S. & Grüner, F. (2011). Imaging laser-wakefield-accelerated electrons using miniature magnetic quadrupole lenses, *Phys. Rev. ST Accel. Beams*, 14(5): 052801.

Wang, X., Zgadzaj, R., Henderson, W., Yi, A. S., Kalmykov, S., Khudik, V., d'Avignon, E., Dong, P., Fazel, N., Korzekwa, R., Chang, Y.-Y., Tsai, Hai-En, Dyer, G., Gaul, E., Martinez, M., Borger, T., Aymond, F., Hammond, D., Escamilla, R., Marijanovic, S., Shvets, G., Ditmire, T. & Downer, M. C. (2011). Self-injected petawatt laser-driven plasma electron acceleration in 10^{17} cm^{-3} plasma, in *Quantum Electronics and Laser Science Conference*, Baltimore, Maryland, OSA Technical Digest (CD) (Optical Society of America, 2011), paper QMJ3; *http://www.opticsinfobase.org/abstract.cfm?URI=QELS-2011-QMJ3*

Wu, H.-C., Xie, B.-S., Liu, M.-P., Hong, X.-R., Zhang, S. & Yu, M. Y. (2009). Electron trajectories and betatron oscillation in the wake bubble in laser-plasma interaction, *Phys. Plasmas* 16(7): 073108.

Xu, H., Yu, W., Lu, P., Senecha, V. K., He, F., Shen, B., Qian, L., Li, R., & Xu, Z. (2005). Electron self-injection and acceleration driven by a tightly focused intense laser beam in an underdense plasma, *Phys. Plasmas* 12(1): 013105.

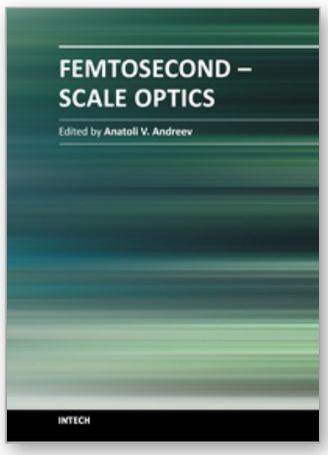

Femtosecond-Scale Optics
Edited by Prof. Anatoly Andreev

ISBN 978-953-307-769-7
Hard cover, 434 pages
Publisher InTech
Published online 14, November, 2011
Published in print edition November, 2011

With progress in ultrashort ultraintense laser technologies the peak power of a laser pulse increases year by year. These new instruments accessible to a large community of researchers revolutionized experiments in nonlinear optics because when laser pulse intensity exceeds or even approaches intra-atomic field strength the new physical picture of light-matter interaction appears. Laser radiation is efficiently transformed into fluxes of charged or neutral particles and the very wide band of electromagnetic emission (from THz up to x-rays) is observed. The traditional phenomena of nonlinear optics as harmonic generation, self-focusing, ionization, etc, demonstrate the drastically different dependency on the laser pulse intensity in contrast the well known rules. This field of researches is in rapid progress now. The presented papers provide a description of recent developments and original results obtained by authors in some specific areas of this very wide scientific field. We hope that the Volume will be of interest for those specialized in the subject of laser-matter interactions.

How to reference
In order to correctly reference this scholarly work, feel free to copy and paste the following:

Serguei Y. Kalmykov, Bradley A. Shadwick, Arnaud Beck and Erik Lefebvre (2011). Physics of Quasi-Monoenergetic Laser-Plasma Acceleration of Electrons in the Blowout Regime, Femtosecond-Scale Optics, Prof. Anatoly Andreev (Ed.), ISBN: 978-953-307-769-7, InTech, Available from: http://www.intechopen.com/books/femtosecond-scale-optics/physics-of-quasi-monoenergetic-laser-plasma-acceleration-of-electrons-in-the-blowout-regime

INTECH
open science | open minds

InTech Europe
University Campus STeP Ri
Slavka Krautzeka 83/A
51000 Rijeka, Croatia
Phone: +385 (51) 770 447
Fax: +385 (51) 686 166
www.intechopen.com

InTech China
Unit 405, Office Block, Hotel Equatorial Shanghai
No.65, Yan An Road (West), Shanghai, 200040, China
中国上海市延安西路65号上海国际贵都大饭店办公楼405单元
Phone: +86-21-62489820
Fax: +86-21-62489821

IntechOpen